

Supporting Information

An Internal Encapsulating Layer for Efficient, Stable, Repairable and Low-lead-leakage Perovskite Solar Cells

*Dongdong Xu, ^a Runsheng Mai, ^a Yue Jiang, ^{*a} Cong Chen, ^{a,b} Ru Wang, ^a Zhengjie Xu, ^a Krzysztof Kempa, ^c Guofu Zhou, ^d Jun-Ming Liu, ^{a, e} Jinwei Gao ^{*a}*

a. Institute for Advanced Materials and Guangdong Provincial Key Laboratory of Optical Information Materials and Technology, South China Academy of Advanced Optoelectronics, South China Normal University, Guangzhou 510006, China.

b. Department of Mechanical Engineering, The University of Hong Kong, Pokfulam Rd., Pokfulam, Hong Kong.

c. Department of Physics, Boston College, Chestnut Hill, Massachusetts 02467, USA.

d. Guangdong Provincial Key Laboratory of Optical Information Materials and Technology & Institute of Electronic Paper Displays, South China Academy of Advanced Optoelectronics, South China Normal University, Guangzhou 510006, China.

e. Laboratory of Solid-State Microstructures, Nanjing University, Nanjing 210093, China.

E-mail: yuejiang@m.scnu.edu.cn (Y.J.), gaojinwei@m.scnu.edu.cn (J.G.)

Contents

1. Experimental procedures

1.1 Materials

1.2 Device Fabrication

2. Characterization

3. Synthetic details

Scheme S1. Synthetic route of Spiro-PU.

Fig. S1. Schematic illustration of the Spiro-PU IEL spin-coating process.

4. Optical, electrochemical, and thermal properties.

Fig. S2. Comparison of the ^1H NMR spectra (DMSO- d_6) of Spiro-OH, NDI and Spiro-NPU.

Fig. S3. (a) Schematic diagram of low solubility of Spiro-NPU (even in 1,1,3,3,3-Hexafluoro-2-propanol (HFIP) with high polarity). (b) GPC determination of prepolymer solution of Spiro-NPU.

Fig. S4. DSC and TGA curves.

Fig. S5. (a) Emission spectra, and (b) UV-vis of Spiro-OH, Spiro-PPU and Spiro-NPU.

Fig. S6. *Tauc* plot of the Spiro-OH, Spiro-PPU and Spiro-NPU.

Fig. S7. UPS spectra of Spiro-OH, Spiro-PPU and Spiro-NPU.

Fig. S8. CV curves of Spiro-OH, Spiro-PPU and Spiro-NPU.

Table S1. Optical, electrochemical properties of Spiro-OH, Spiro-PPU and Spiro-NPU.

Fig. S9. Band-edges of the stacked films in the device.

Fig. S10. Top-view AFM images of $\text{CH}_3\text{NH}_3\text{PbI}_3$ without and with Spiro-NPU.

Fig. S11. SCLC curves.

Table S2. TRPL fitting results.

5. Device performance

Fig. S12. The statistical distributions of 20 devices based on $\text{CH}_3\text{NH}_3\text{PbI}_3$ absorber.

Fig. S13. $J-V$ characteristics of the best-performing based on $\text{CH}_3\text{NH}_3\text{PbI}_3$ absorber.

Table S3. The average $J-V$ performance of $\text{CH}_3\text{NH}_3\text{PbI}_3$ -based PSCs manufactured with different precursor concentrations. (The values are obtained from 20 independent devices)

Fig. S14. EQE spectra and integrated photocurrent curves of the corresponding devices.

Fig. S15. The statistical distributions of 30 independent devices

Table S4. The average $J-V$ performance of $\text{Cs}_{0.05}\text{FA}_{0.85}\text{MA}_{0.10}\text{Pb}(\text{Br}_{0.03}\text{I}_{0.97})_3$ -based PSCs manufactured with different precursor concentrations.

Fig. S16. ^1H NMR spectra of **Spiro-NPU** with or without PbI_2 . The NMR reference chemical shift is the tetramethylsilane (TMS).

Fig. S17. (a) The dark current–voltage curves. (b) V_{oc} dependence on light intensity. (c) Dark J – V curves. (d) Nyquist plots.

Fig. S18. The water contact angle of perovskite/Spiro-NPU.

Fig. S19. One solar irradiation recovery.

Fig. S20. Heating recovery.

Fig. S21. Schematic illustration of the degradation and repairable mechanism.

Fig. S22. (a) The statistical distributions of 10 devices based on FTO/ $\text{CH}_3\text{NH}_3\text{PbI}_3$ /Spiro-NPU/Spiro-OMeTAD/Au under various conditions. (b) J – V curves of the champion devices.

Fig. S23. Stabilized power output measurement.

Fig. S24. XPS spectra after FTO/Spiro-NPU/Li-TFSI+tBP device aging.

Fig. S25. (a) Photographs of the $\text{CH}_3\text{NH}_3\text{PbI}_3$ film with **Spiro-NPU** soaking in water. (b) XRD patterns of the $\text{CH}_3\text{NH}_3\text{PbI}_3$ /Spiro-NPU film soaking in water for 30 minutes.

Fig. S26. (a) Photographs of the $\text{CH}_3\text{NH}_3\text{PbI}_3$ films without and with Spiro-NPU soaking in water for a long time. (b) Determination of Pb^{2+} concentration in water at different soaking time.

Fig. S27. Cross-sectional SEM image of the completed device.

6. Properties of Spiro-PPU and devices.

Fig. S28. Fourier-transform infrared (FTIR) spectra of Spiro-OH, PPDI and Spiro-PPU.

Fig. S29. (a) Top-view AFM and (b) SEM image of Spiro-PPU. (c) Water contact angles on the surface of Spiro-PPU.

Fig. S30. The statistical distributions with Spiro-PPU.

Table S5. The average J – V performance of $\text{CH}_3\text{NH}_3\text{PbI}_3$, or $\text{Cs}_{0.05}\text{FA}_{0.85}\text{MA}_{0.10}\text{Pb}(\text{Br}_{0.03}\text{I}_{0.97})_3$ -based PSCs manufactured with Spiro-PPU.

Fig. S31. J – V curves of the champion devices with Spiro-PPU.

Fig. S32. The steady-state photocurrent measurements at maximum power point.

Fig. S33. J – V curve of flexible PSCs based on $\text{Cs}_{0.05}\text{FA}_{0.85}\text{MA}_{0.10}\text{Pb}(\text{Br}_{0.03}\text{I}_{0.97})_3$ PSCs.

Fig. S34. Bending cycles of flexible devices.

Fig. S35. Steady-state PL and TRPL spectra about Spiro-PPU.

7. ^1H NMR, ^{13}C NMR and HR-MS spectra.

1. Experimental procedures

1.1 Materials

All chemicals and reagents used for synthesis were purchased commercially (Aladdin and energy chemical) and used directly without any further purification. Solvents were purified by standard methods and dried if necessary. Reactions were monitored by thin layer chromatography (TLC) and were carried out under argon atmosphere. The materials and super dehydrated solvents used for perovskite solar cell fabrication were all purchased from Advanced Election Technology Co. Ltd., Xi'an Polymer Light Technology Corp, Yingkou Libra New Energy Technology Co. Ltd., and Sigma-Aldrich. Air-sensitive reactions were carried out under nitrogen atmosphere. The device preparation was done in a glovebox under nitrogen atmosphere.

1.2 Device Fabrication

SnO₂ NCs solution was prepared by our previous method.¹ The perovskite precursor solution of MAPbI₃ was prepared by dissolving 922 mg PbI₂ and 318 mg MAI in 1.6 mL mixed solvent of DMF and DMSO (7:3). The perovskite precursor solution of Cs_{0.05}FA_{0.85}MA_{0.10}Pb(Br_{0.03}I_{0.97})₃ was prepared by dissolving 742.2 mg PbI₂, 224.4 mg FAI, 16.2 mg MABr, 20.3 mg MACl and 19.8 mg CsI in 1 mL mixed solvent of DMF and DMSO (4:1). Spiro-OMeTAD solution was prepared by dissolving 72mg Spiro-OMeTAD into 1 ml chlorobenzene, with the dopant of 17.5 μL Li-TFSI solution (520 mg in 1 mL acetonitrile), 28.8 μL tBP.

FTO substrates were sequentially ultrasonically cleaned with detergent, deionized water and isopropanol for 10 min. The substrates were further cleaned with UV ozone treatment for 15 min before used. Then the SnO₂ NCs solution was dropped on the FTO substrates and spin-coated at 500 rpm for 3 s and 3000 rpm for 30 s, followed by thermal annealing at 150 °C for 1 h. The MAPbI₃-perovskite precursor solution was spin-coated on SnO₂ layer at 500 rpm for 3 s and 4000 rpm for 30 s. And 420 μL chlorobenzene as antisolvent was dripped onto the perovskite film 21 s prior to the end of the second spinning program. As well as the Cs_{0.05}FA_{0.85}MA_{0.10}Pb(Br_{0.03}I_{0.97})₃-perovskite precursor solution was spin-coated at 1000 rpm for 10 s and 5000 rpm for 30 s. And 100 μL chlorobenzene as antisolvent was dripped onto the perovskite film 10 s prior to the end of the second spinning program. After that, the Spiro-PU solutions were deposited onto the perovskite layers by spin-coating at 3000 rpm for 30 s at 85 °C.

Then, the Spiro-OMeTAD solutions were deposited onto the perovskite layers by spin-coating at 3000 rpm for 30 s. Finally, 100 nm thick film of Ag was thermally evaporated under high vacuum on top of the hole transporting layer. and the active area of all devices is 0.07 cm² defined by a metal mask.

2. Characterization

¹H NMR and ¹³C NMR spectra were recorded with a Bruker-600MHz spectrometer. Mass spectra were obtained by Bruker ultrafle Xtreme MALDITOF/TOF. The thermal decomposition temperature (T_d) was confirmed by thermogravimetric analysis (TGA) from PerkinElmer Pyris 1 conducted under N₂ atmosphere at a heating rate of 10 °C min⁻¹ from 25 °C to 800 °C. The differential scanning calorimetry (DSC) was conducted on Mettler Toledo DSC 1 instrument at heating rate of 10 °C min⁻¹ under nitrogen atmosphere within temperature range of 0 °C to 160 °C. We measured three cycles of DSC, and the second cycle is reported.

The electrochemical cyclic voltammetry (CV) was conducted on an electrochemical workstation (CHI760D Chenhua, Shanghai) with Pt plate as working electrode, Pt slice as counter electrode, and saturated calomel electrode (SCE) as reference electrode in tetrabutylammonium hexafluorophosphate (*n*-Bu₄NPF₆, 0.1 M) dichloromethane solutions at a scan rate of 100 mV s⁻¹. In addition, the insoluble Spiro-PU was coated on Pt plate as working electrode for testing. Ferrocene/ferrocenium (Fc/Fc⁺) was used as the reference. UV-vis absorption spectra of Spiro-OH in THF solution (10⁻⁵ mol/L) and thin film on quartz (spin-coated Spiro-OH and Spiro-PU in CB, 3000 rpm for 20s) were recorded with a PerkinElmer lambda 950 UV/Vis/NIR Spectrophotometer. Photoluminescence (PL) spectra of Spiro-OH in THF solution (10⁻⁵ mol/L) and thin film on quartz (spin-coated Spiro-OH and Spiro-PU in CB, 3000 rpm for 20s) were measured with a HITACHI F-4600 spectrofluorometer.

GPC gel permeation chromatograph was used to determine the molecular weight of **Spiro-NPU** precursor solution, model Waters 1515. We have designed an experiment to gauge the cross-linking efficiency of **Spiro-NPU**. We soaked the as-obtained **Spiro-NPU** (x mg) with CB (20 mL) overnight and conducted the vacuum filtration, followed by drying and measuring the left materials (y mg). We define the ration of y/x as the cross-linking efficiency. We also collected five groups of independent experimental data and calculated their average value.

The morphology and microstructures were investigated by FE-SEM (ZEISS Ultra-500). The

J–V characteristics of the devices were measured with a Keithley 2440 source under a simulated AM1.5G spectrum. With a solar simulator (Newport, 91160), the light intensity was calibrated using a standard silicon solar cell device by the NREL. The external quantum efficiency (EQE) curves were measured using a standard EQE system (Newport 66902), consist of a xenon light source, a monochromator, and a potentiostat. The surface roughness was measured by atomic-force microscopy (AFM). The X-Ray Diffraction (XRD) was measured using X-ray polycrystalline diffractometer (BRUKER D8 ADVANCE). The electrochemical impedance spectroscopy (EIS) measurements were performed on the Zahner Zennium electrochemical workstation with an illumination of 300 W m⁻² light source. Steady-state photoluminescence emission spectroscopy (PL) and time-resolved photoluminescence (TRPL) were measured by fluorescence spectrometer (HITACHI F-5000) and steady-state/transient fluorescence spectrometer (FLS980) with the excitation wavelength of 450 nm.

Hole mobility was measured by using the space-charge-limited current (SCLC) method with the device structure of ITO/PEDOT:PSS/Spiro-PU/Spiro-OMeTAD/Ag. Space charge-limited current can be described by equation below:

$$J = \frac{9\mu\epsilon_r\epsilon_0 V^2}{8D^3}$$

where J is the current density, μ is the hole mobility, ϵ_0 is the vacuum permittivity (8.85×10^{-12} F/m), ϵ_r is the dielectric constant of the material (normally taken to approach 3.5 for organic semiconductors), V is the applied bias, d is the film thickness of the active layer is obtained from cross-sectional SEM. When plotted on a log-log plot the J - V characteristics will ideally exhibit three characteristic regimes: In the range of low voltage, the current increases linearly with the increase of the voltage, indicating an Ohmic response. At intermediate voltages, the current exhibited a rapid non-linear increase, indicating the trap-controlled space charge limited current. At higher voltage the current exhibited a $J \propto V^2$ behavior, indicating trap-filled SCLC region according to Mott Gurney law.

J - V characteristics of the devices was measured using a Keithley 2400 in the dark. The devices configuration follows: ITO/PEDOT:PSS/Perovskite/Spiro-PU/Spiro-OMeTAD/Ag for hole-only devices, and ITO/Perovskite /Ag for electron-only devices. The perovskite films and

Spiro-OMeTAD films were made by the same protocols used in solar cell fabrication. PEDOT:PSS films were prepared by spin-coated PEDOT:PSS aqueous solution on ITO at 4000 rpm for 30 s, and then baked at 120 °C for 15 min according to SCLC theory, the defect (trap) density can be estimated as follows:

$$n_{trap} = \frac{2\varepsilon\varepsilon_0V_{TFL}}{eL^2}$$

where L , ε , ε_0 and e are the thickness of the perovskite film, dielectric constant of the material, permittivity of vacuum, and electronic charge, respectively.

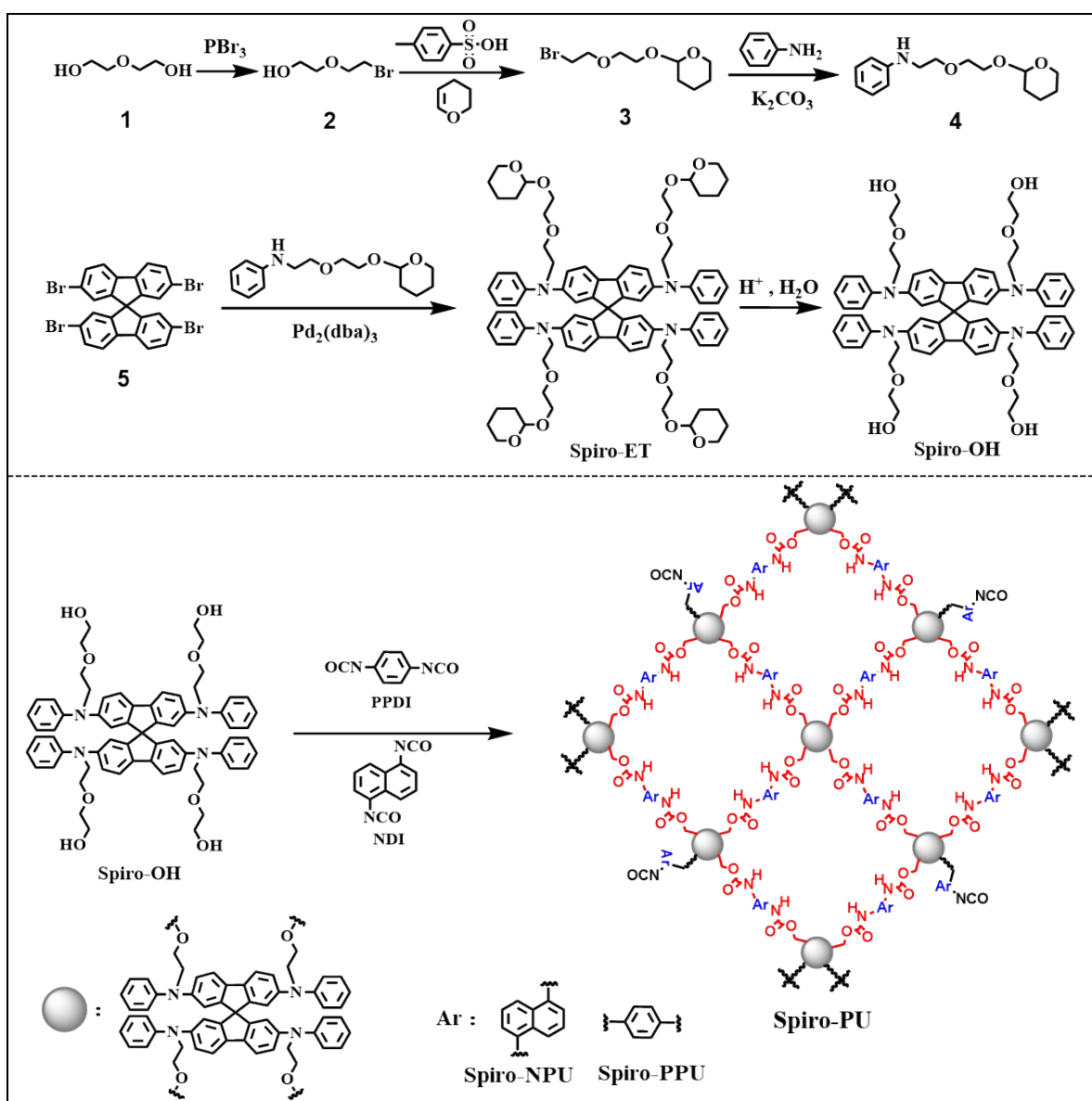
XPS spectra was performed for films on silicon wafers using a Thermo Fisher ESCALAB 250 Xi. Curve fitting was performed using the Thermo Avantage software. The curves were corrected based on the C1s peak at 284.8 eV. The samples were prepared by spin-coating 20 μ L of the perovskite colloidal precursor solution (same solution used in the fabrication process of PSCs) on silicon wafer. UPS spectra were recorded by Thermo Fisher ESCALAB 250Xi, with a He I α source ($h\nu=21.22$), an ultrahigh vacuum chamber with a base pressure of $\sim 10^{-10}$ torr.

Flame atomic absorption spectrophotometry (FAAS) was conducted with an ZA3000 (HITACHI, JAPAN), equipped with a Pb hollow-cathode lamp as a radiation source, where the resonance line wavelength is 217 nm. A calibration curve based on PbI₂ solutions was referenced by all sample tests to determine the aqueous Pb content in pure water as a standard.

Desktop constant temperature and humidity testing machine was conducted with a T-TOPH-22-C (TOTC TEST EQRATION CO., LIMITED).

TOF-SIMS measurement was performed using a TOF-SIMS V instrument (ION-TOF GmbH 5, Münster, Germany), where a 3 keV Cs⁺ ion beam was used for erosion and a 25 keV Bi⁺ pulsed primary ion beam was used for the analysis. The area of analysis was 104 \times 104 μ m² while the sputtering area was 260 \times 260 μ m²

3. Synthetic details



Scheme S1. Synthetic route of Spiro-PU.

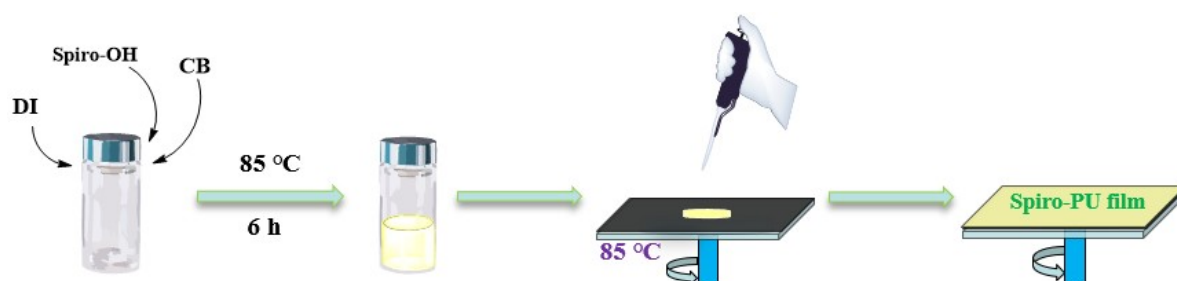


Fig. S1. Schematic illustration of the Spiro-PU IEL spin-coating process.

2-(2-bromoethoxy)ethan-1-ol (2). Phosphorus tribromide (3.15 g, 11.5 mmol) was dropwise to diethylene glycol (10.6g, 100 mmol) at -5 °C for 0.5h. The reaction mixture was slowly warmed to room temperature and heated to 160 °C for 2 hours. The crude material was purified by column chromatography (EtAc:PE = 2:1) to give oil in 48% yield (8 g, 47.6 mmol). ¹H NMR (600 MHz, CDCl₃-d₁): 4.19 (s, 1H), 3.70-3.56 (m, 8H).

2-(2-(2-bromoethoxy)ethoxy)tetrahydro-2H-pyran (3). To solution of 2-(2-bromoethoxy)ethanol (7.05 g, 42 mmol) in CHCl₂ (70 mL) were added 3,4-dihydro-2H-pyran (3.87 g, 46 mmol) and a catalytic amount of toluenesulfonic acid (70 mg) and the mixture was allowed to stir at room temperature for 6 h. The reaction mixture was washed with H₂O and evaporated under reduced pressure to give the product as an oil in 53% yield (4 g, 15.9 mmol). ¹H NMR (600 MHz, CDCl₃-d₁): 4.54 (s, 1H), 3.77-3.40 (m, 10H). ¹³C NMR (150 MHz, CDCl₃-d₁): 98.74, 72.48, 70.41, 66.55, 61.94, 61.52, 30.45, 25.35, 19.29.

N-(2-(2-((tetrahydro-2H-pyran-2-yl)oxy)ethoxy)ethyl)aniline (4). Aniline (1.48 g, 15.9 mmol) was dissolved in DMF (10 ml) in round-bottom flask. To this stirred solution (3) (4 g, 15.9 mmol) and K₂CO₃ (5.5 g, 40 mmol) were added. Then, the reaction mixture was heated to 70 °C stir for 36 h. Solvent was removed under reduced pressure and the residue was extracted three times with CHCl₂. The combined organic layers were dried over anhydrous sodium sulphate. After removing the solvent, the crude product was purified by passing through a silica column using ethylacetate /hexane (1:4) as the eluent to as a yellow liquid in 72% yield (3 g, 11.3 mmol). ¹H NMR (600 MHz, CDCl₃-d₁): 7.22-7.19 (t, *J*=12Hz, 2H), 6.74-6.65 (m, 3H), 4.67-4.66 (t, *J*=6Hz, 1H), 3.92-3.32 (m, 10H), 1.86-1.55 (m, 6H). ¹³C NMR (150 MHz, CDCl₃-d₁): 148.32, 132.90, 117.71, 113.13, 99.05, 70.28, 69.53, 62.32, 43.10, 30.62, 25.47, 19.47.

N₂,N₂',N₇,N₇'-tetraphenyl-N₂,N₂',N₇,N₇'-tetrakis(2-(2-((tetrahydro-2H-pyran-yl)oxy)ethoxy)ethyl)-9,9'-spirobi[fluorene]-2,2',7,7'-tetraamine (Spiro-ET). A mixture of (5) (0.5 g, 0.8 mmol), (4) (1.27 g, 4.8 mmol), t-BuONa (0.2 g, 2.08mmol), Pd₂(dba)₃ (0.03 g, 0.032 mmol), tri-tert-butylphosphine terafluoroborate (TTBuP) (0.01 g, 0.034 mmol) into dry toluene (10 ml), and heated at 120 °C for 24 h under nitrogen atmosphere. After cooling, it was quenched with water and extracted with dichloromethane. The crude product was purified by passing through silica column to give (Spiro-ET) as a yellow oil (600 mg, 55.4 % yield). ¹H NMR (600 MHz, CDCl₃-d₁): 7.57-7.56 (d, *J*=6Hz, 1H), 7.14-7.12 (t, *J*=12Hz, 2H), 7.05-7.04 (d, *J*=6Hz, 1H), 6.84-6.83

(d, $J=6\text{Hz}$, 1H), 6.80-6.77 (t, $J=12\text{Hz}$, 2H), 6.56 (s 1H), 4.57-4.55 (t, $J=12\text{Hz}$, 1H), 3.81-73.74 (m, 4H), 3.60-3.44 (m, 6H), 1.78-1.48 (m, 6H). ^{13}C NMR (150 MHz, $\text{CDCl}_3\text{-d}_1$): 150.37, 148.08, 146.59, 136.35, 129.01, 122.98, 120.27, 119.81, 118.43, 98.94, 70.52, 67.98, 66.66, 62.16, 51.62, 30.53, 25.43, 19.46. Mass spectrometry (HRMS-ESI, m/z): $[\text{M}+\text{H}]^+$ calcd. for $\text{C}_{85}\text{H}_{100}\text{N}_4\text{O}_{12}$: 1368.73; found: 1368.79.

2,2',2'',2'''-(((9,9'-spirobifluorene)-2,2',7,7'-tetrayltetrakis(phenylazanediy))tetrakis(ethane-2,1-diy))tetrakis(oxy))tetrakis(ethan-1-ol) (Spiro-OH). To a solution of (**Spiro-ET**) (500mg, 0.365mmol), THF 3mL, methanol 15mL and toluenesulfonic acid (63mg, 0.365mmol) at room temperature (RT) for 12 h. Then add Na_2CO_3 solution to adjust the pH to neutral, add ethyl acetate to extract three times, and purified by column chromatography on silica gel (ethyl acetate : methanol = 15 : 1) to afford a yellow-green solid (230 mg, yield 61%). ^1H NMR (600 MHz, DMSO-d_6): 7.71-7.69 (d, $J=6\text{Hz}$, 1H), 7.14-7.11 (t, $J=18\text{Hz}$, 2H), 7.05-7.03 (d, $J=12\text{Hz}$, 1H), 6.84-6.80 (M, 3H), 6.34 (s, 1H), 4.52-4.50 (t, $J=12\text{Hz}$, 1H), 3.76-3.74 (t, $J=12\text{Hz}$, 2H), 3.48-3.46 (t, $J=12\text{Hz}$, 2H), 3.77-3.75 (t, $J=12\text{Hz}$, 2H), 3.28-3.26 (t, $J=12\text{Hz}$, 2H). ^{13}C NMR (150 MHz, DMSO-d_6): 150.51, 147.94, 146.88, 136.25, 129.16, 122.83, 120.26, 118.78, 118.29, 72.35, 68.28, 61.67, 51.64. Mass spectrometry (HRMS-ESI, m/z): $[\text{M}+\text{H}]^+$ calcd. for $\text{C}_{65}\text{H}_{68}\text{N}_4\text{O}_8$: 1032.50; found: 1032.48. ($T_g = 35\text{ }^\circ\text{C}$, $T_d = 390\text{ }^\circ\text{C}$)

The optimal Spiro-NPU prepolymer solution was prepared by dissolving 20 mg Spiro-OH and 12.6 mg 1,5-Naphthalene Diisocyanate (NDI) in 1 mL chlorobenzene (CB), and then stirred at $85\text{ }^\circ\text{C}$ for 6 h. The remaining exploratory concentrations were 10 mg Spiro-OH (6.3 mg NDI) and 30 mg Spiro-OH (18.9 mg NDI), and Spiro-PPU was prepared by 20 mg Spiro-OH and 9.2 mg PDI. We call Spiro-PU of PPDI as **Spiro-PPU** ($T_g = 137\text{ }^\circ\text{C}$, $T_d = 175\text{ }^\circ\text{C}$), and Spiro-PU of NDI as **Spiro-NPU** ($T_g = 125\text{ }^\circ\text{C}$, $T_d = 170\text{ }^\circ\text{C}$).

The polymer power of **Spiro-NPU** could not be dissolved, thus the GPC determination of prepolymer solution of **Spiro-NPU** was conducted ($M_p = 87145$, $M_n = 39576$, $M_v = 77497$, $M_w = 84488$, $M_z = 134725$, $M_{z+1} = 180112$, $PD = 2.1348$). The cross-linking efficiency was determined to be 98%.

4. Optical, electrochemical, and thermal properties.

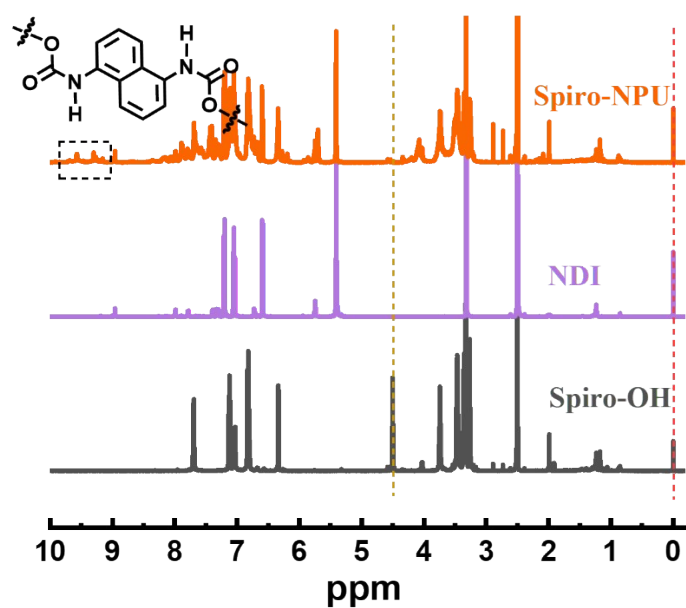
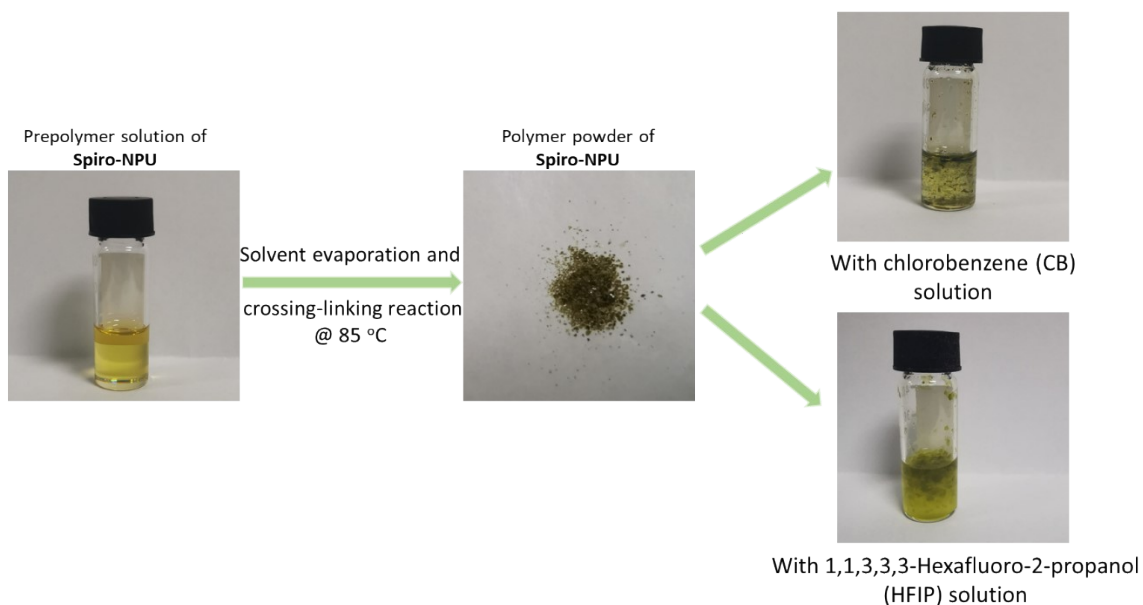


Fig. S2. Comparison of the ¹H NMR spectra (DMSO-d₆) of Spiro-OH, NDI and Spiro-NPU. Spiro-OH and NDI were dissolved in DMSO-d₆ for heating polymerization to obtain the Spiro-NPU.

a**b****MW Averages**

Mp: 87145

Mn: 39576

Mv: 77497

Mw: 84488

Mz: 134725

Mz+1: 180112

PD: 2.1348

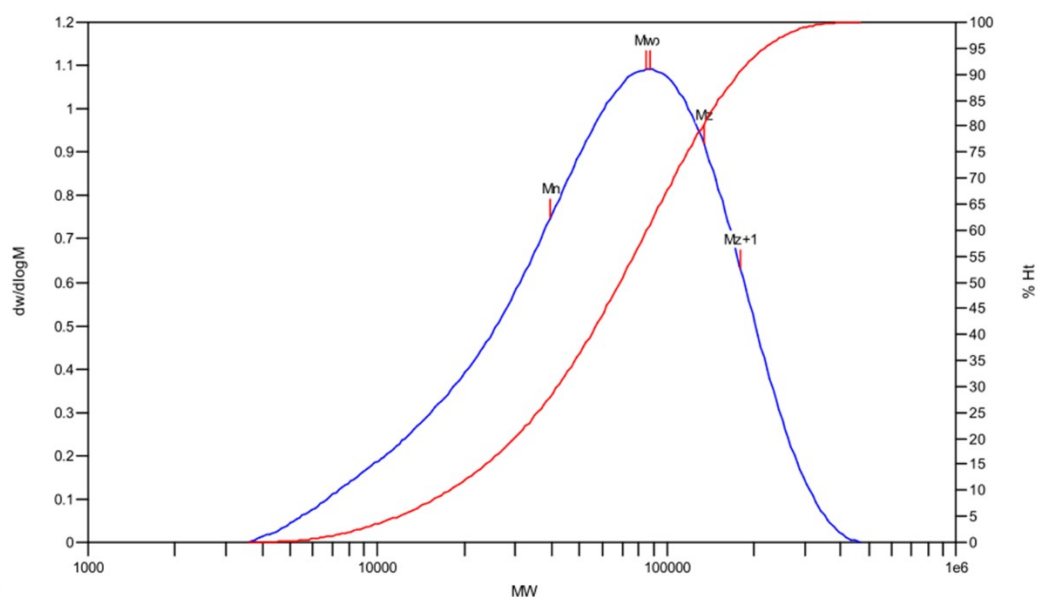
Distribution Plots

Fig. S3. (a) Schematic diagram of low solubility of Spiro-NPU (even in 1,1,3,3,3-Hexafluoro-2-propanol (HFIP) with high polarity). (b) GPC determination of prepolymer solution of Spiro-NPU.

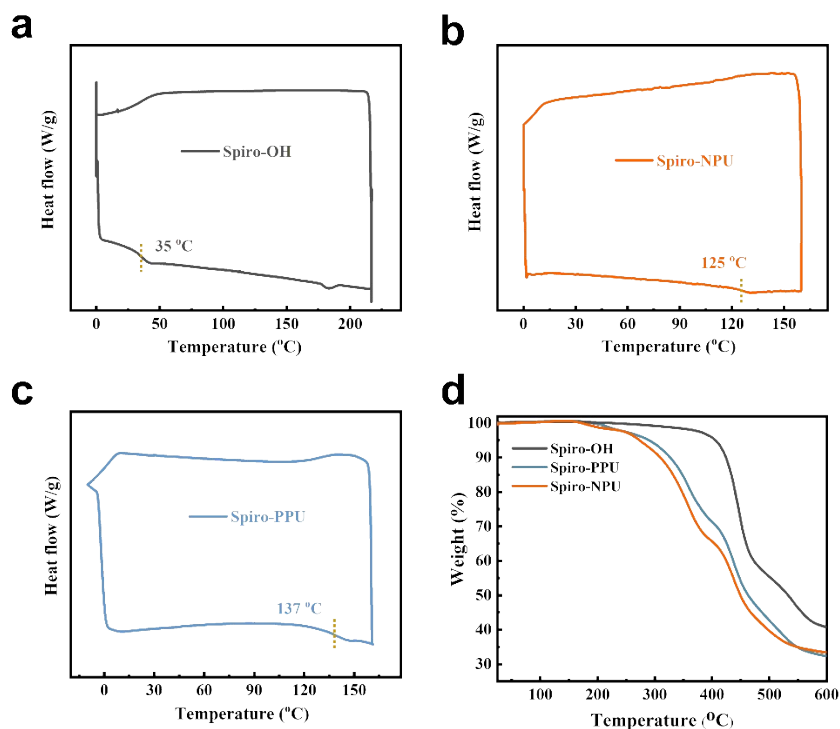


Fig. S4. (a-c) DSC curve of Spiro-OH, Spiro-NPU and Spiro-PPU, respectively. (d) TGA curves of Spiro-OH, Spiro-NPU and Spiro-PPU, respectively. (The decomposition temperature is about 170 °C, which is due to the -NCO group.)

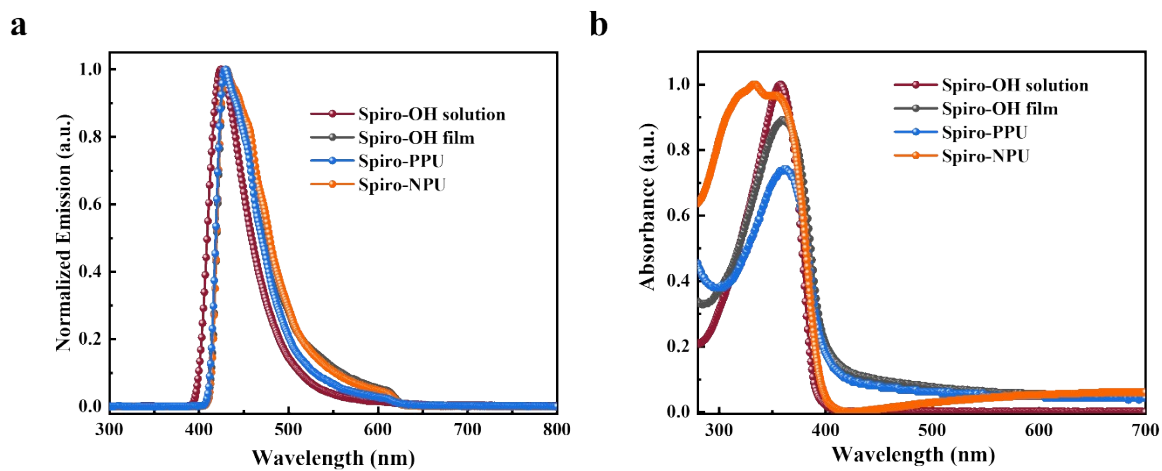


Fig. S5. (a) Emission spectra, and (b) UV-vis of Spiro-OH, Spiro-PPU and Spiro-NPU.

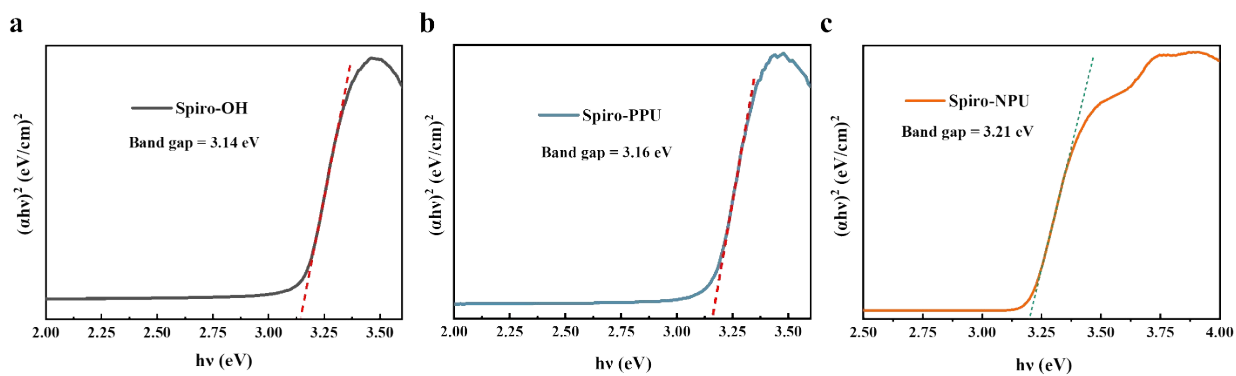


Fig. S6. Tauc plot of the Spiro-OH, Spiro-PPU and Spiro-NPU.

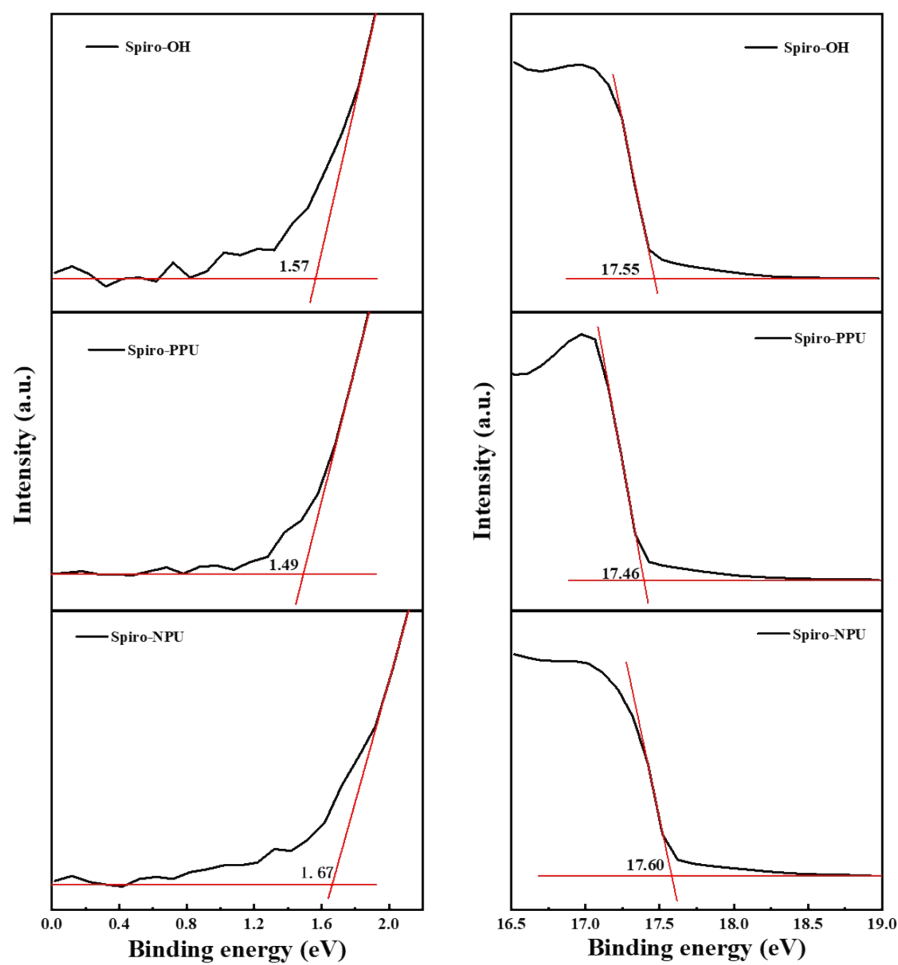


Fig. S7. UPS spectra of Spiro-OH, Spiro-PPU and Spiro-NPU.

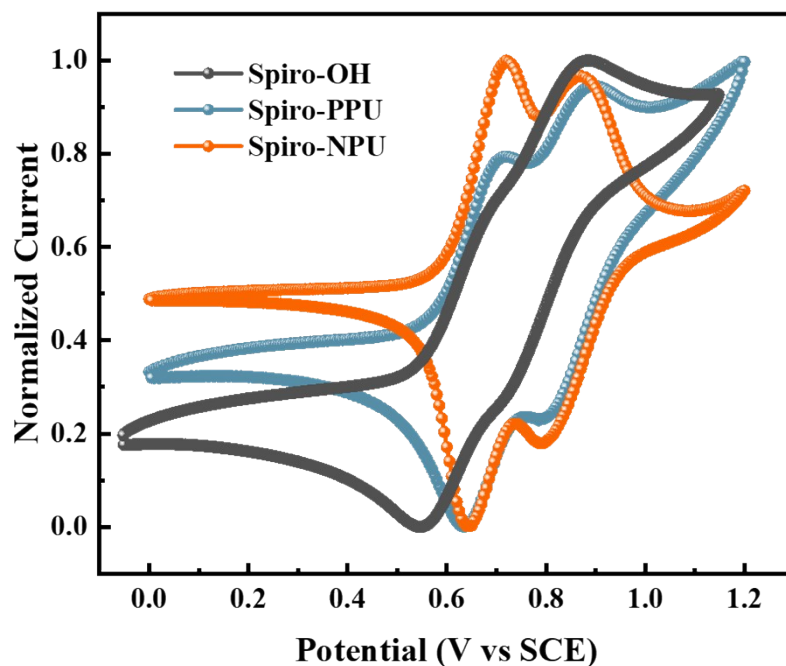


Fig. S8. CV curves of Spiro-OH, Spiro-PPU and Spiro-NPU.

Table S1. Optical, electrochemical properties of Spiro-OH, Spiro-PPU and Spiro-NPU.

Sample	λ_{\max} (nm)	λ_{em} (nm)	E_g (eV)	E_{HOMO} (eV)	E_{LUMO} (eV)
Spiro-OH	356.99 ^s 359.09 ^f	424.48 ^s 428.93 ^f	3.14	-5.26* -5.24	-2.12* -2.20
Spiro-PPU	360.63	428.93	3.16	-5.27* -5.25	-2.11* -2.09
Spiro-NPU	353.83	428.93	3.21	-5.32* -5.29	-2.11* -2.08

^sResults from Absorption in THF solution. ^fResults from absorption of films. *Results from CV curves.

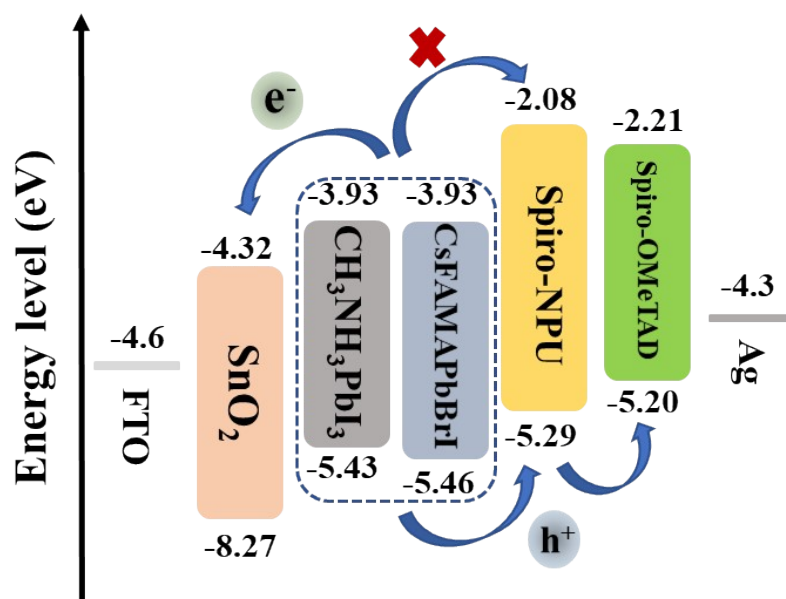


Fig. S9. Band-edges of the stacked films in the device.

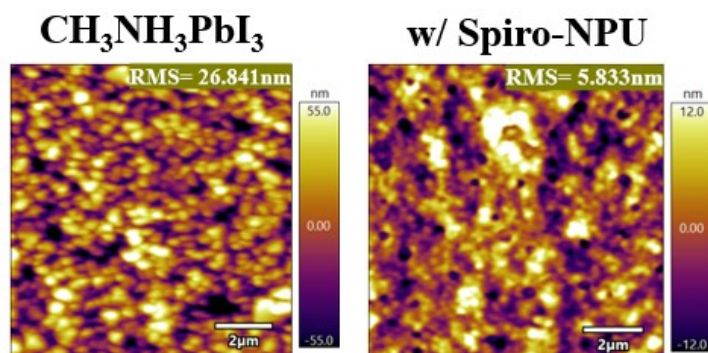


Fig. S10. Top-view AFM images of CH₃NH₃PbI₃ without and with Spiro-NPU

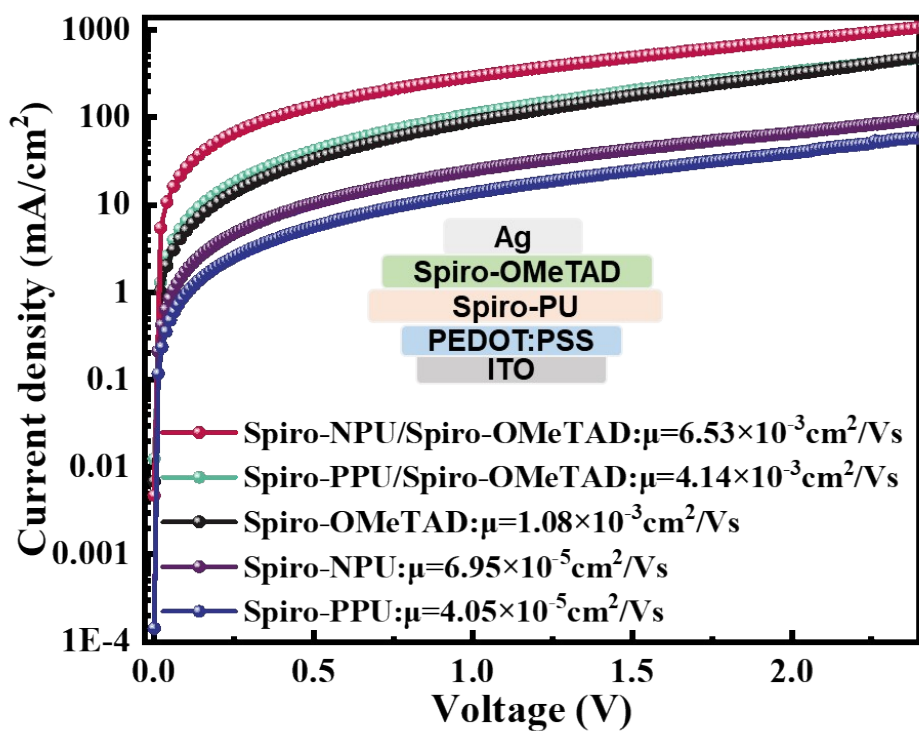


Fig. S11. SCLC curves.

Table S2. TRPL fitting results.

Samples	$\tau_{\text{ave}}(\text{ns})$	$\tau_1(\text{ns})$	A_1	$\tau_2(\text{ns})$	A_2
PVK	114.43	25.37	8.58	116.25	91.42
PVK/Spiro-PPU	77.29	15.08	58.99	91.96	41.01
PVK/Spiro-NPU	57.09	12.88	74.09	77.97	25.91
PVK/Spiro-OMeTAD	26.61	6.97	95.91	71.51	4.09
PVK/Spiro-PPU/ Spiro-OMeTAD	19.08	10.47	84.98	34.06	15.02
PVK/Spiro-NPU/ Spiro-OMeTAD	10.19	5.33	94.93	27.69	5.07

5. Device performance

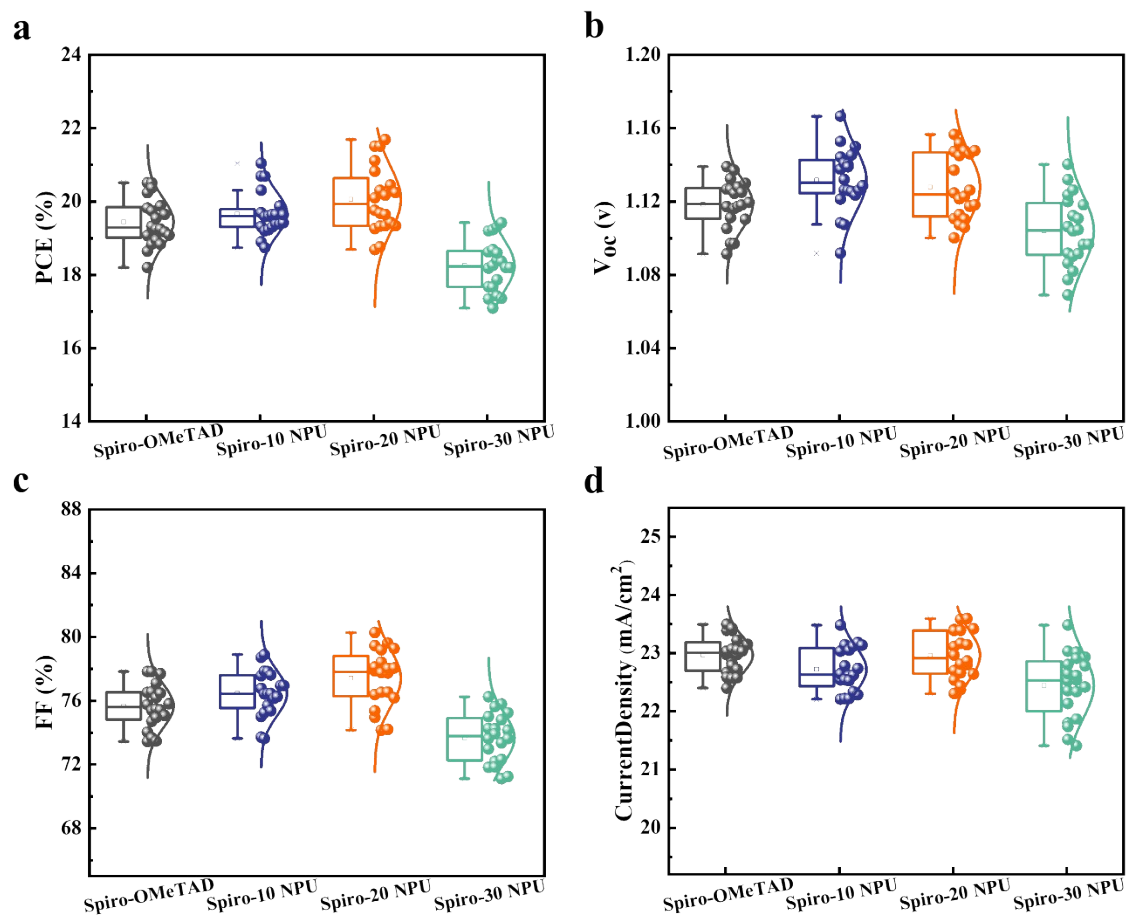


Fig. S12. The statistical distributions of 20 devices based on $\text{CH}_3\text{NH}_3\text{PbI}_3$ with different concentration of Spiro-NPU of (a) *PCE*, (b) V_{oc} , (c) *FF*, and (d) J_{sc}

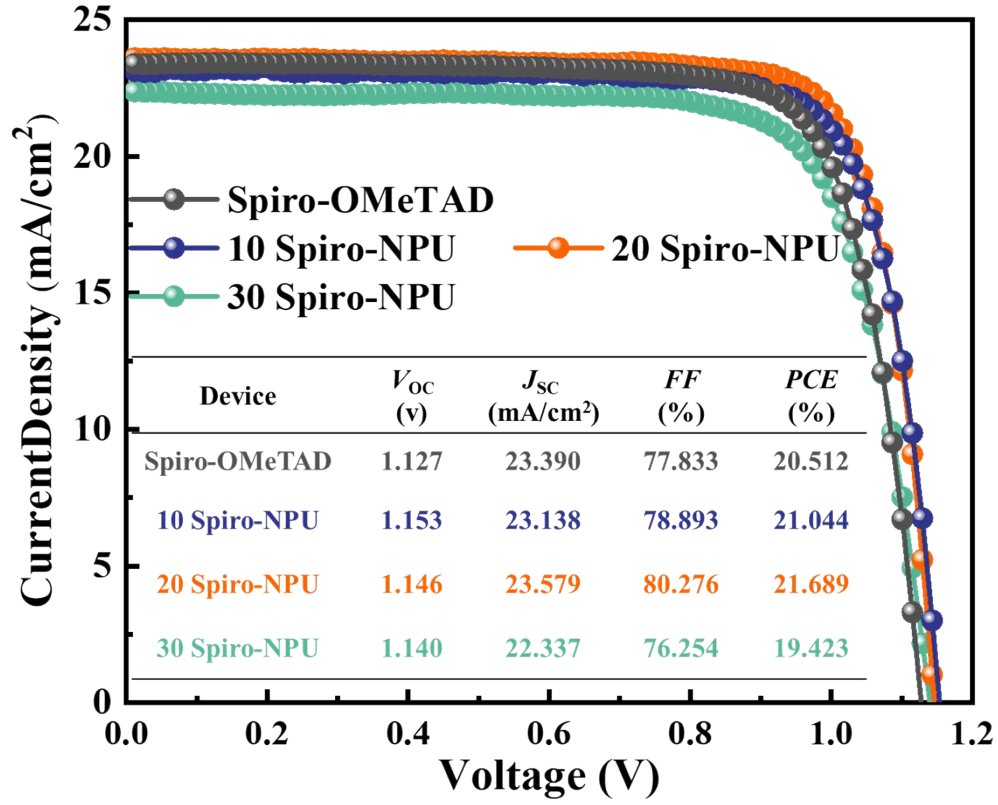


Fig. S13. J - V characteristics of the best-performing based on $\text{CH}_3\text{NH}_3\text{PbI}_3$.

Table S3. The average J - V performance of $\text{CH}_3\text{NH}_3\text{PbI}_3$ -based PSCs manufactured with different precursor concentrations. (The values are obtained from 20 devices)

Device	V_{oc} (v)	J_{sc} (mA/cm ²)	FF (%)	PCE (%)
Spiro-OMeTAD	1.118±0.013	22.988±0.355	75.638±1.334	19.453±0.658
10 Spiro-NPU	1.132±0.017	22.722±0.380	76.480±1.430	19.666±0.597
20 Spiro-NPU	1.128±0.018	22.965±0.411	77.407±1.804	20.058±0.899
30 Spiro-NPU	1.104±0.019	22.444±0.554	73.676±1.544	18.256±0.670

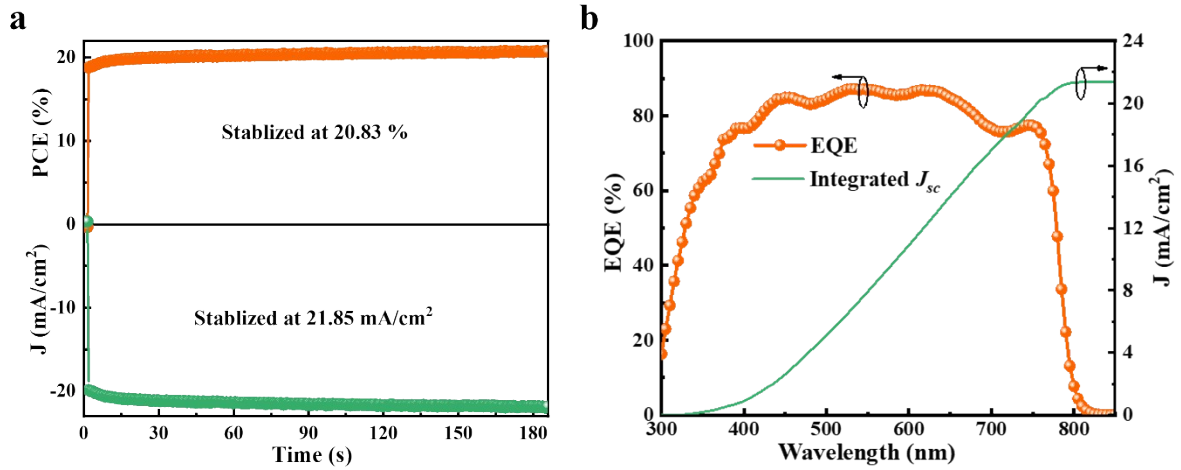


Fig. S14. (a) The steady-state output at maximum power point for $\text{CH}_3\text{NH}_3\text{PbI}_3$ with Spiro-NPU. (b) EQE spectra and integrated photocurrent curves of the corresponding devices

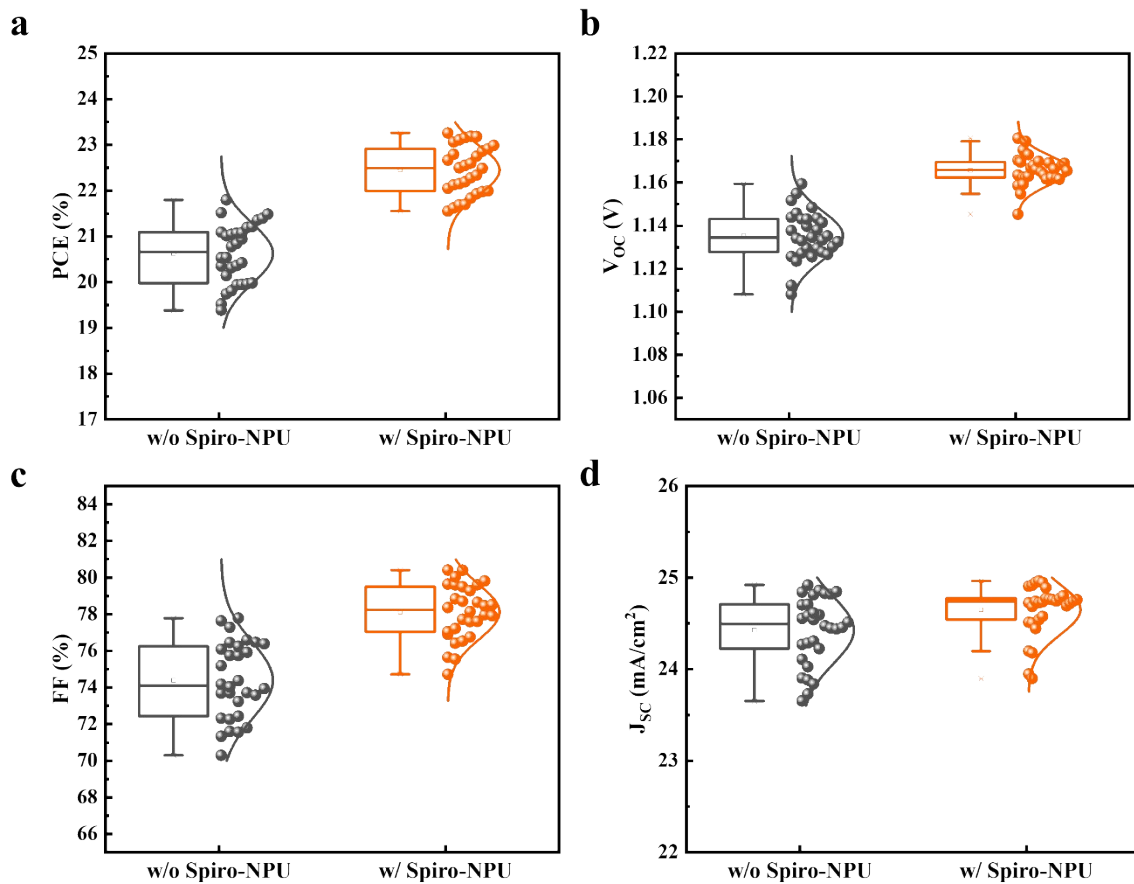


Fig. S15. The statistical distributions of 30 devices based on $\text{Cs}_{0.05}\text{FA}_{0.85}\text{MA}_{0.10}\text{Pb}(\text{Br}_{0.03}\text{I}_{0.97})_3$ with or without Spiro-NPU of (a) PCE , (b) V_{OC} , (c) FF , and (d) J_{SC} .

Table S4. The average J - V performance of $\text{Cs}_{0.05}\text{FA}_{0.85}\text{MA}_{0.10}\text{Pb}(\text{Br}_{0.03}\text{I}_{0.97})_3$ -based PSCs manufactured with different precursor concentrations. (The values are obtained from 30 devices)

Device	V_{OC} (v)	J_{SC} (mA/cm ²)	FF (%)	PCE (%)
w/o Spiro-NPU	1.135±0.011	24.426±0.366	74.386±2.084	20.627±0.651
w/ Spiro-NPU	1.166±0.007	24.650±0.275	78.119±1.489	22.459±0.532

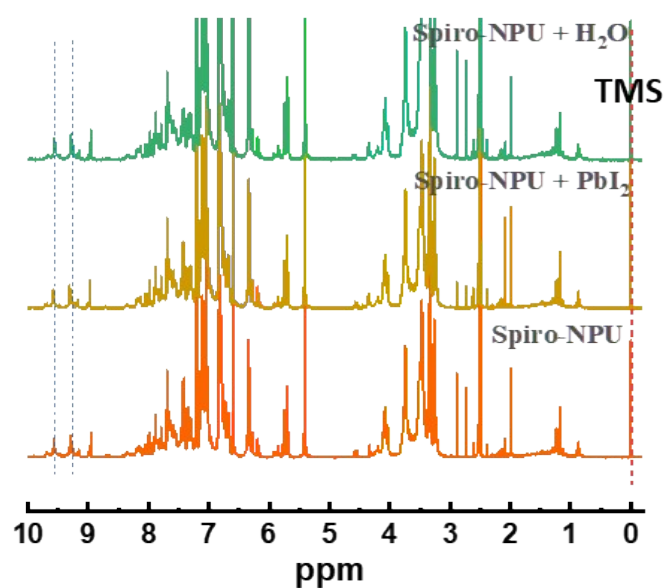


Fig. S16. ¹H NMR spectra of Spiro-NPU with or without PbI₂. The NMR reference chemical shift is the tetramethylsilane (TMS).

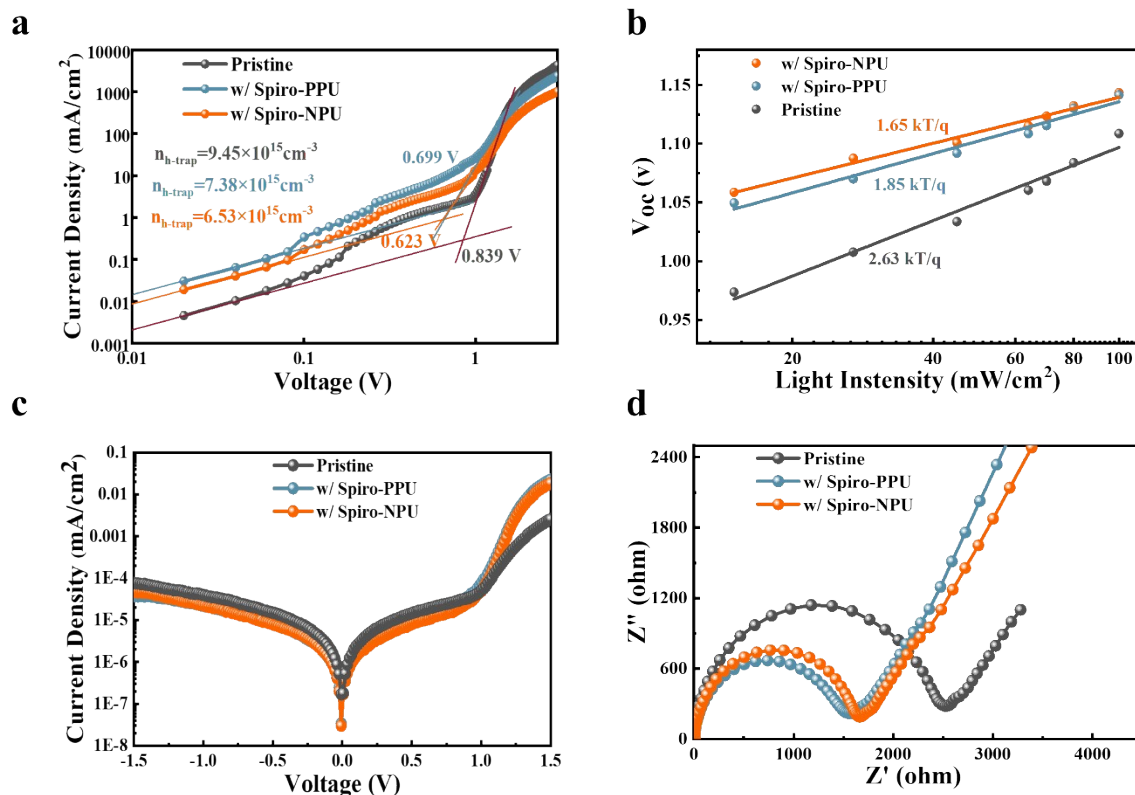


Fig. S17. (a) The dark current–voltage curves for hole-only devices of ITO/PEDOT:PSS/perovskite/Spiro-PU/Spiro-OMeTAD/Ag. (b) Voc dependence on light intensity. (c) Dark J–V curves. (d) Nyquist plots of PSCs under the dark condition at 0.7 V bias.

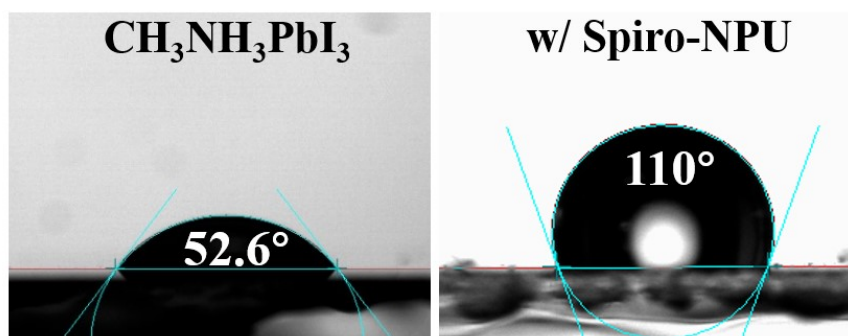


Fig. S18. The water contact angle of perovskite/Spiro-NPU.

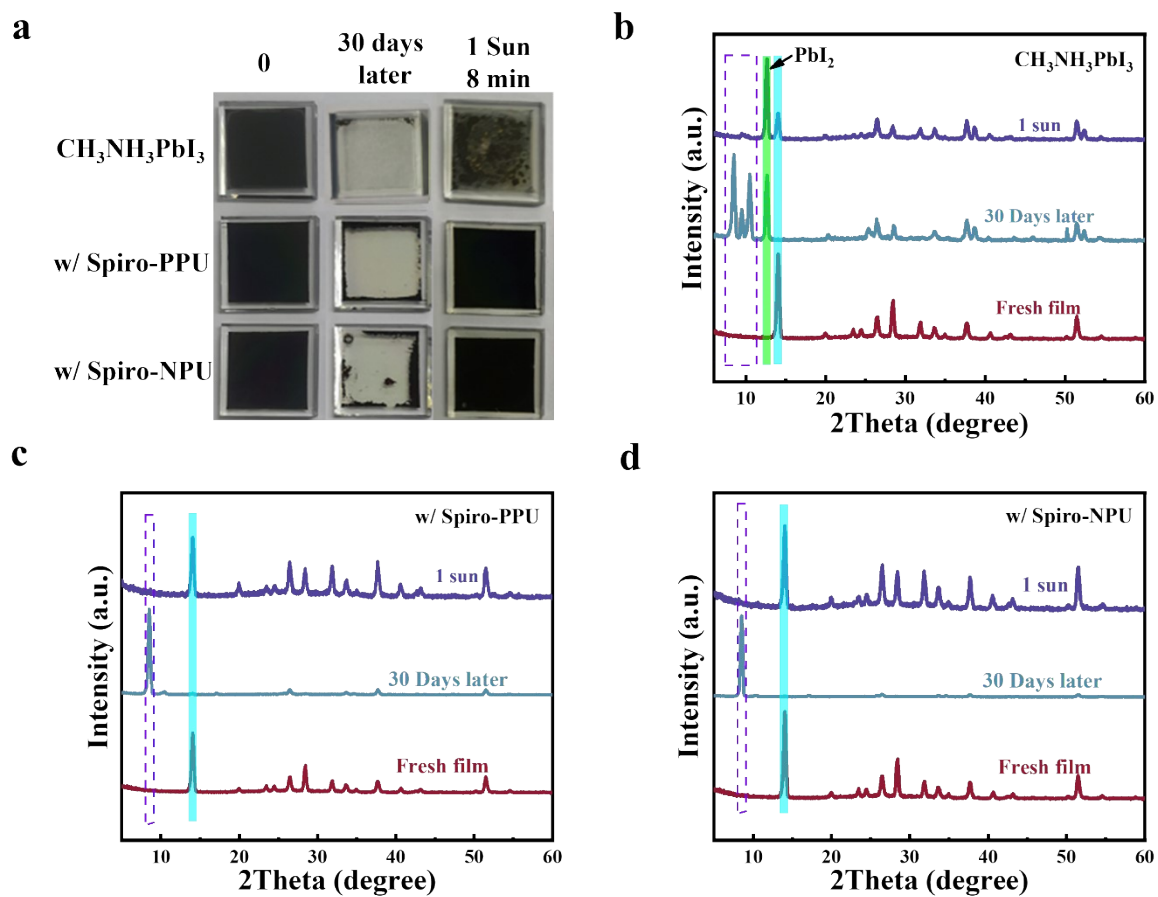


Fig. S19. (a) Photographs of the $\text{CH}_3\text{NH}_3\text{PbI}_3$ films with and without Spiro-PU exposed to 85 % RH for 30 days and 8 min irradiation at one sun. (b-d) Corresponding XRD patterns of the $\text{CH}_3\text{NH}_3\text{PbI}_3$ films with and without polymer.

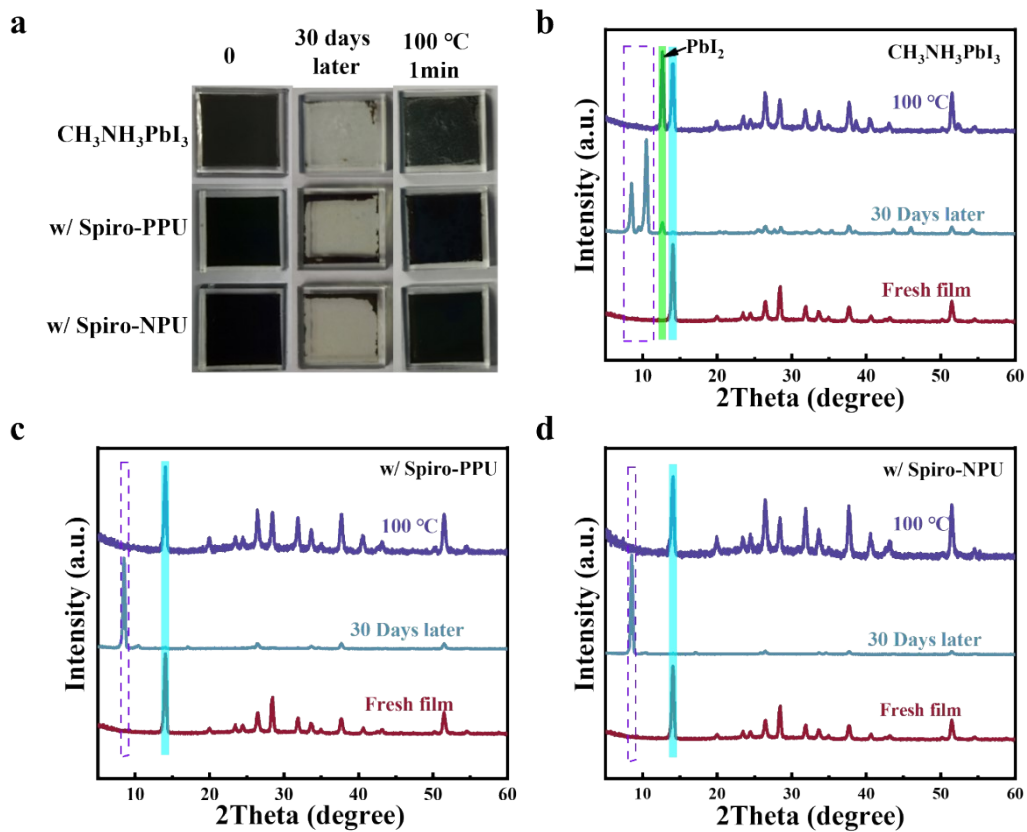


Fig. S20. (a) Photographs of the $\text{CH}_3\text{NH}_3\text{PbI}_3$ films with and without Spiro-PU exposed to 85 % RH for 30 days and thermal annealing at 100 °C for 1 min. (b-d) Corresponding XRD patterns of the $\text{CH}_3\text{NH}_3\text{PbI}_3$ films with and without polymer.

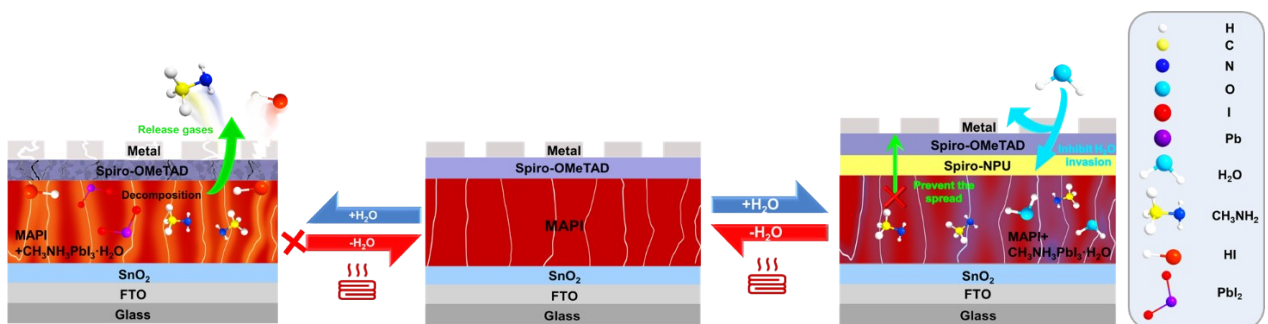


Fig. S21. Schematic illustration of the degradation and repairable mechanism.

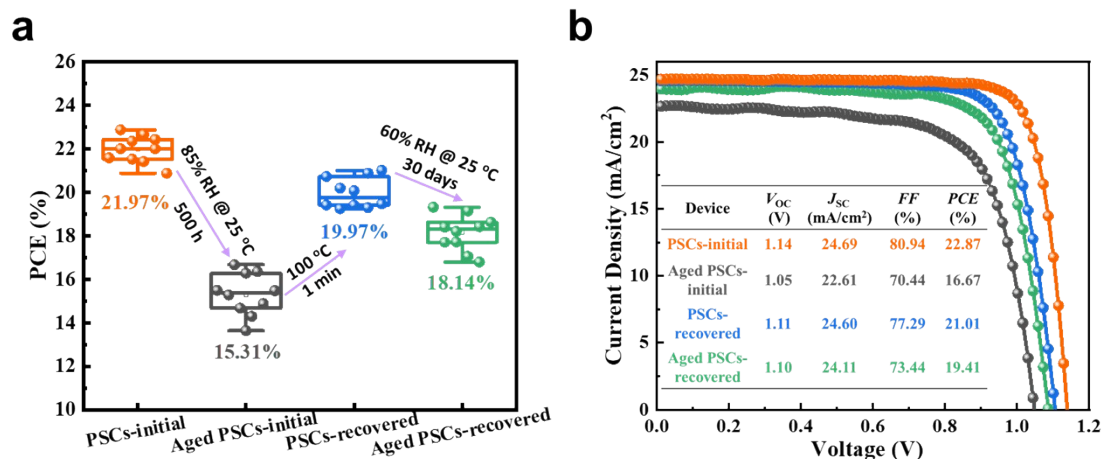


Fig. S22. (a) The statistical distributions of 10 devices based on FTO/SnO₂/Cs_{0.05}FA_{0.85}MA_{0.10}Pb(Br_{0.03}I_{0.97})₃/Spiro-NPU/Spiro-OMeTAD/Au under various conditions. (b) J - V curves of the champion devices.

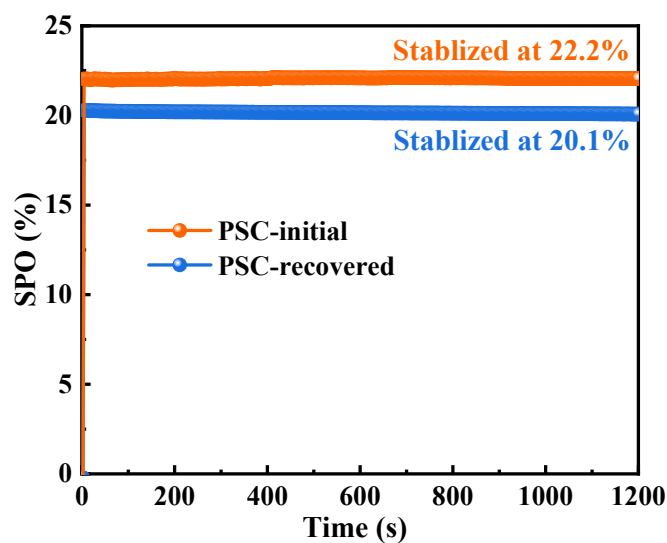


Fig. S23. Stabilized power output measurement of fresh and recovered devices based on FTO/SnO₂/Cs_{0.05}FA_{0.85}MA_{0.10}Pb(Br_{0.03}I_{0.97})₃/Spiro-NPU/Spiro-OMeTAD/Au.

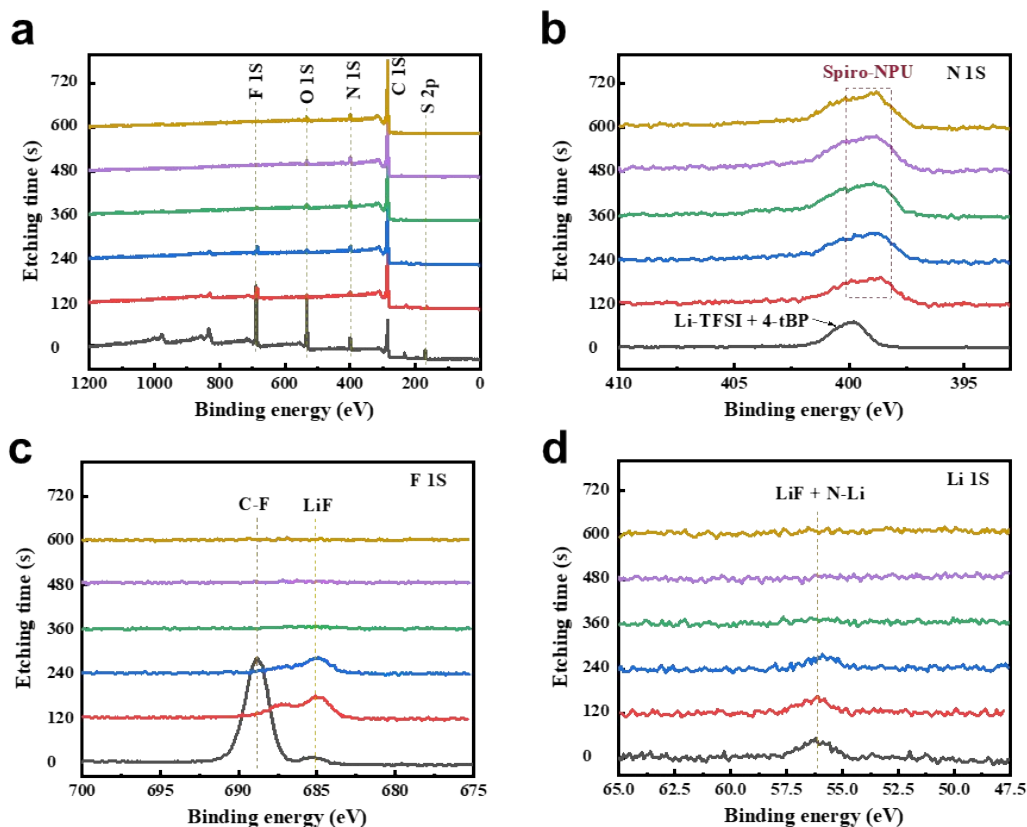


Fig. S24. XPS spectra after FTO/Spiro-NPU/Li-TFSI+tBP device aging. **(a)** survey, **(b)** N 1S, **(c)** F 1S, and **(d)** Li 1S. First, the Spiro-NPU was deposited onto FTO by spin-coating, then a mixture of Li-TFSI and tBP (1 ml chlorobenzene with the dopant of 17.5 μL Li-TFSI solution and 28.8 μL t-BP) deposited onto Spiro-NPU, and finally exposed it to 85% RH (25 $^{\circ}\text{C}$) for 500 hours of aging treatment. We carried out in-depth analysis (Ar^+ , 1 keV) on the aged films with etching time of 0 s, 120 s, 240 s, 360 s, 480 s and 600 s, respectively.

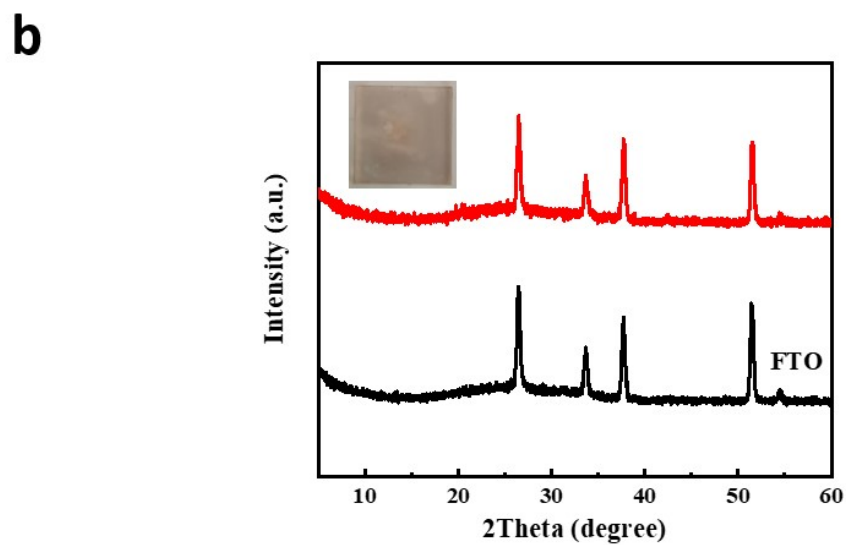
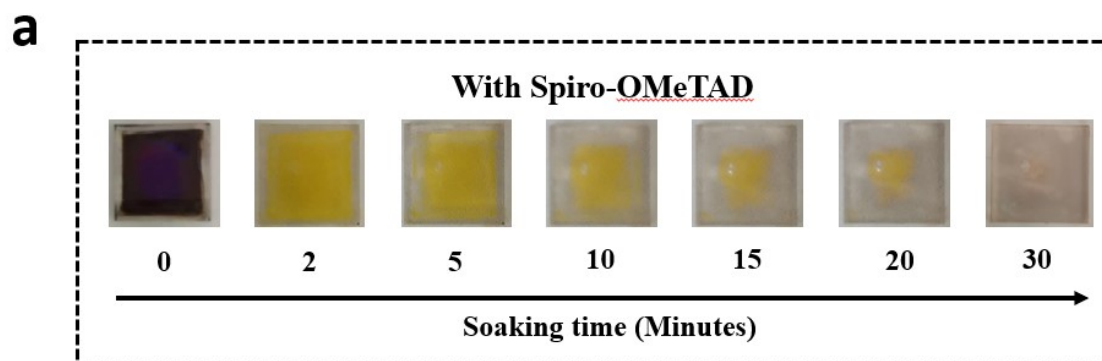


Fig. S25. (a) Photographs of the $\text{CH}_3\text{NH}_3\text{PbI}_3$ film with Spiro-OMeTAD soaked in water. (b) XRD patterns of the $\text{CH}_3\text{NH}_3\text{PbI}_3$ /Spiro-OMeTAD film after soaked in water over 30 minutes.

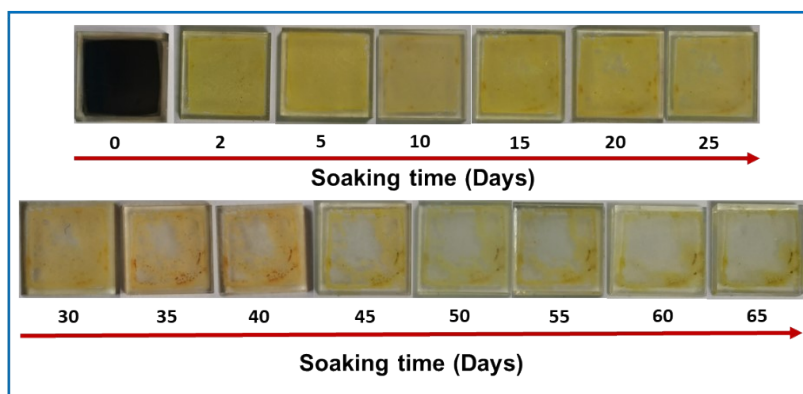
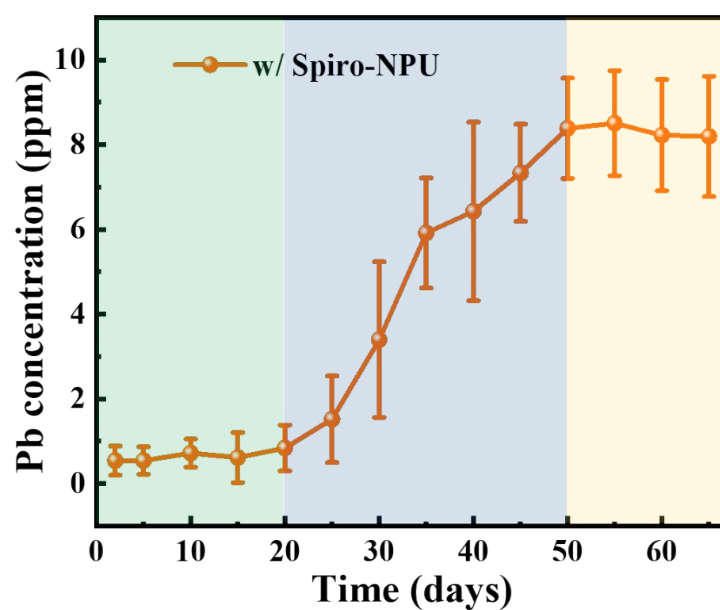
a**b**

Fig. S26. (a) Photographs of the $\text{CH}_3\text{NH}_3\text{PbI}_3$ films without and with Spiro-NPU soaked in water for a long time. (b) Determination of Pb^{2+} concentration in water at different soaking time.

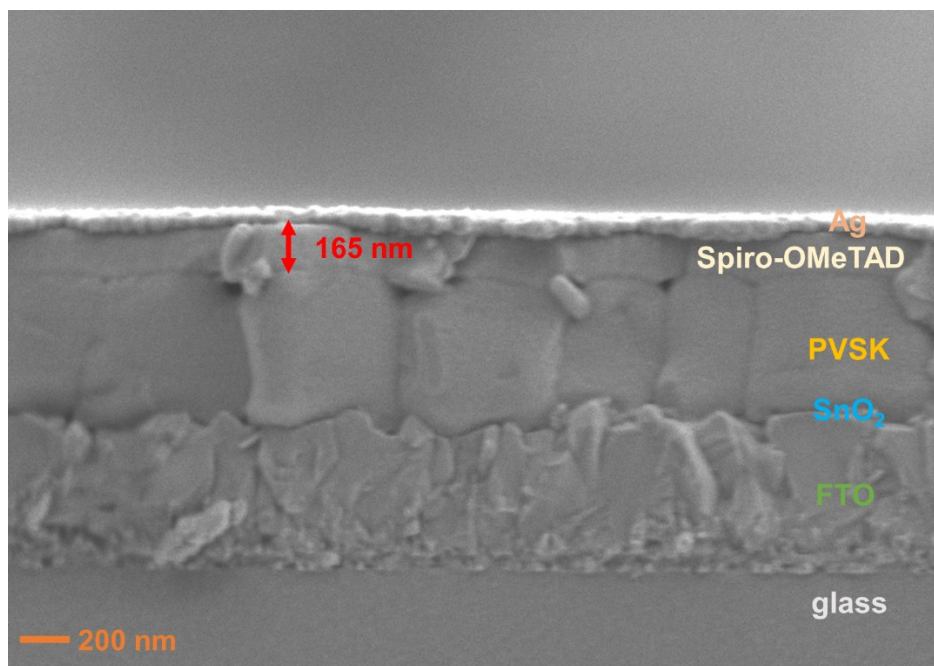


Fig. S27. Cross-sectional SEM image of the completed device.

6. Properties of Spiro-PPU and devices.

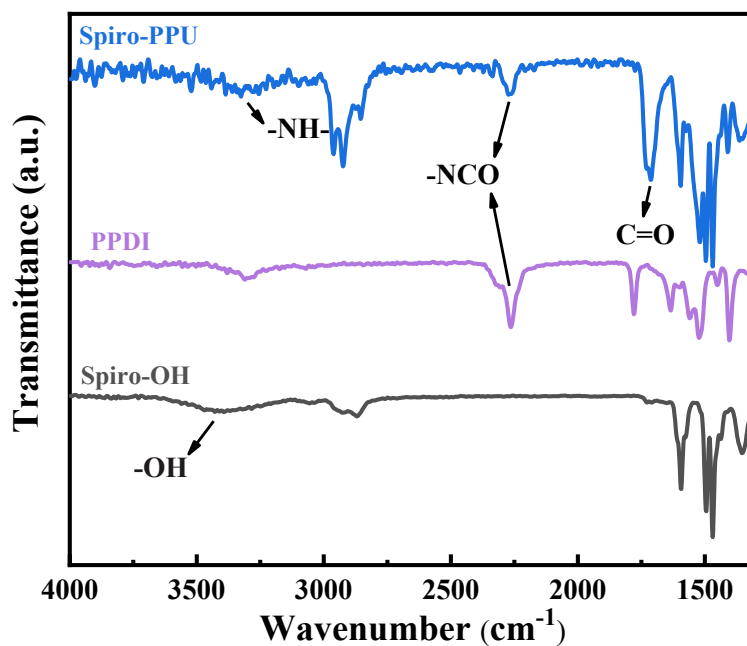


Fig. S28. FTIR spectra of Spiro-OH, PPDI and Spiro-PPU. The C=O stretching vibration at $\sim 1718 \text{ cm}^{-1}$, -NH- stretching vibration at $\sim 3336 \text{ cm}^{-1}$, -NCO stretching vibration at $\sim 2266 \text{ cm}^{-1}$ and -OH stretching vibration at $\sim 3412 \text{ cm}^{-1}$ are marked.

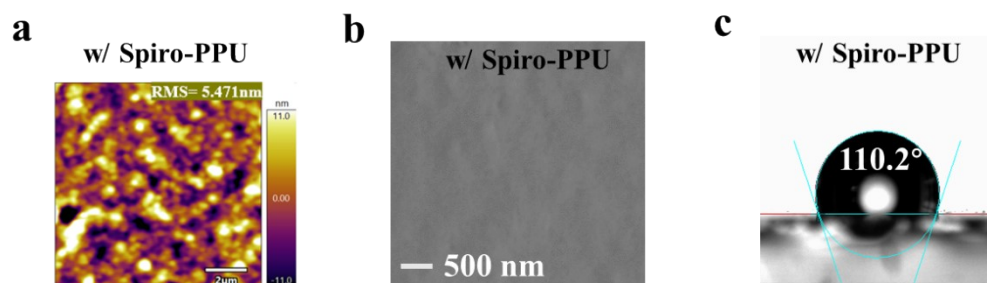


Fig. S29. (a) Top-view AFM and (b) SEM image of Spiro-PPU. (c) Water contact angles on the surface of Spiro-PPU.

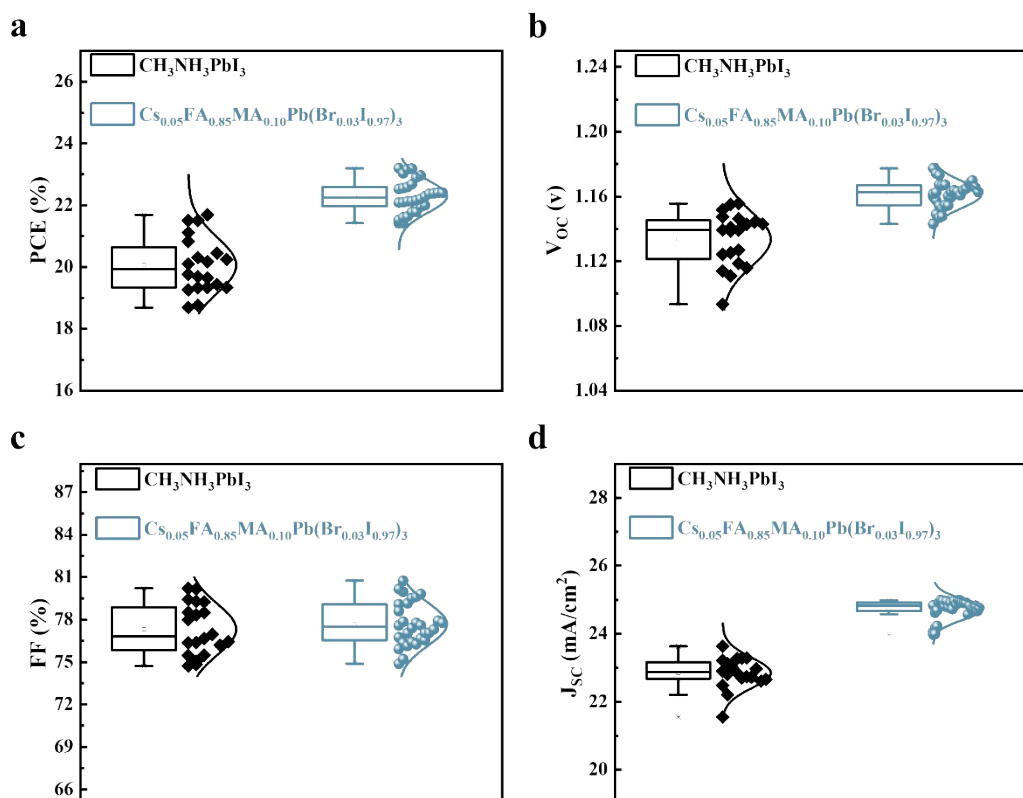


Fig. S30. The statistical distributions of 20 devices based- $\text{CH}_3\text{NH}_3\text{PbI}_3$, and 30 devices based on $\text{Cs}_{0.05}\text{FA}_{0.85}\text{MA}_{0.10}\text{Pb}(\text{Br}_{0.03}\text{I}_{0.97})_3$ with Spiro-PPU of (a) PCE , (b) V_{OC} , (c) FF , and (d) J_{SC} .

Table S5. The average J-V performance of PSCs based on $\text{CH}_3\text{NH}_3\text{PbI}_3$, or $\text{Cs}_{0.05}\text{FA}_{0.85}\text{MA}_{0.10}\text{Pb}(\text{Br}_{0.03}\text{I}_{0.97})_3$ with Spiro-PPU. (The values are obtained from 20 devices for $\text{CH}_3\text{NH}_3\text{PbI}_3$, 30 devices for $\text{Cs}_{0.05}\text{FA}_{0.85}\text{MA}_{0.10}\text{Pb}(\text{Br}_{0.03}\text{I}_{0.97})_3$)

Device (w/ Spiro-PPU)	V_{OC} (v)	J_{SC} (mA/cm^2)	FF (%)	PCE (%)
$\text{CH}_3\text{NH}_3\text{PbI}_3$	1.134 ± 0.017	22.848 ± 0.448	77.309 ± 1.807	20.058 ± 0.899
$\text{Cs}_{0.05}\text{FA}_{0.85}\text{MA}_{0.10}\text{Pb}(\text{Br}_{0.03}\text{I}_{0.97})_3$	1.161 ± 0.008	24.709 ± 0.308	77.673 ± 1.518	22.285 ± 0.526

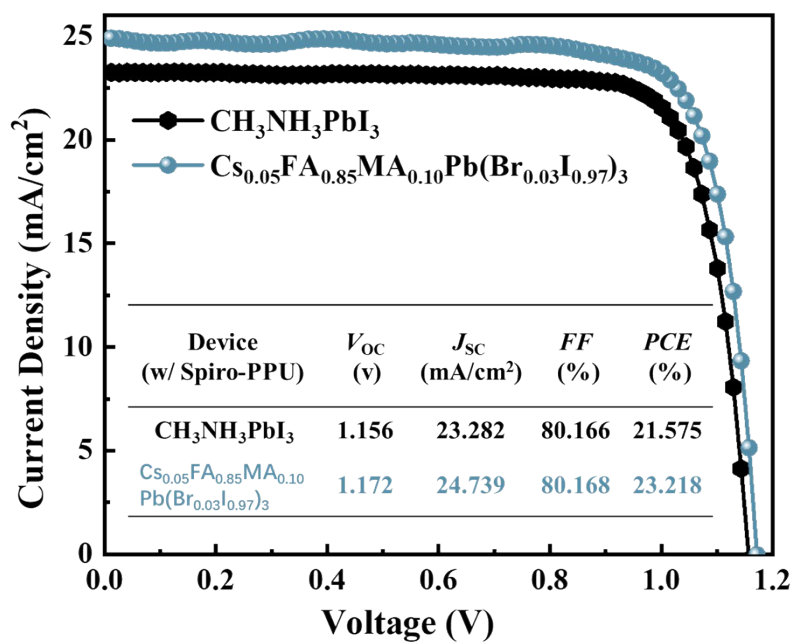


Fig. S31. J - V curves of the champion devices with Spiro-PPU based on Cs_{0.05}FA_{0.85}MA_{0.10}Pb(Br_{0.03}I_{0.97})₃ and CH₃NH₃PbI₃ absorbers, respectively.

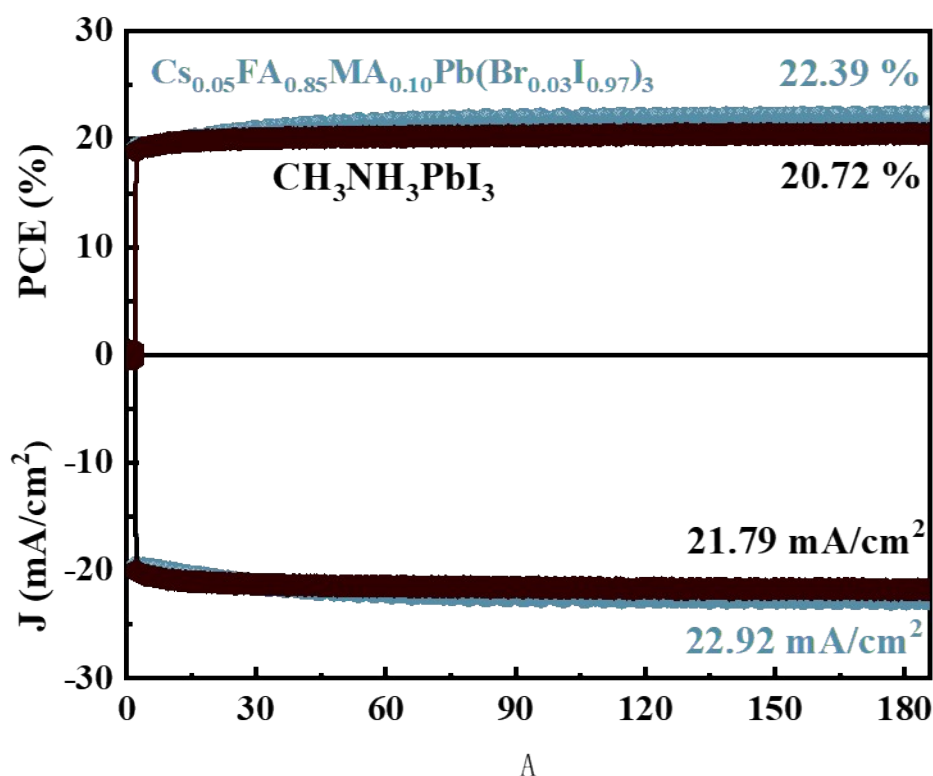


Fig. S32. The steady-state output at maximum power point for PSCs based on CH₃NH₃PbI₃ or Cs_{0.05}FA_{0.85}MA_{0.10}Pb(Br_{0.03}I_{0.97})₃ with Spiro-PPU IEL.

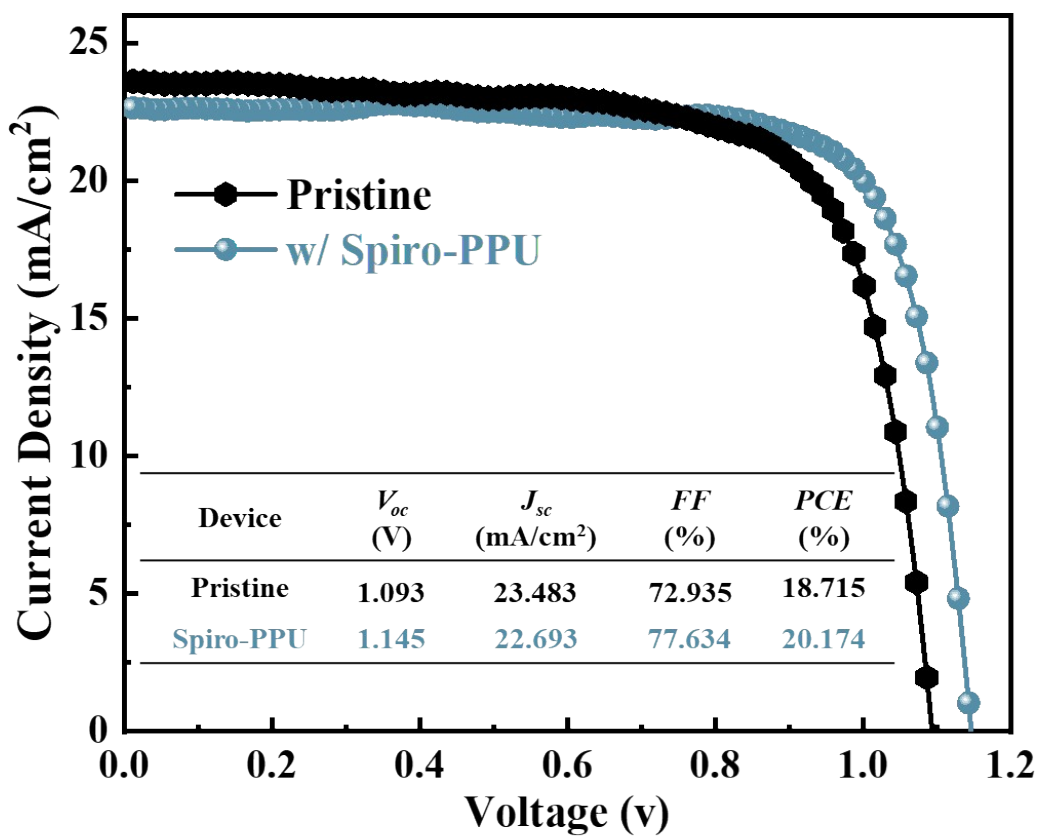


Fig. S33. J - V curve of flexible PSCs based on $Cs_{0.05}FA_{0.85}MA_{0.10}Pb(Br_{0.03}I_{0.97})_3$.

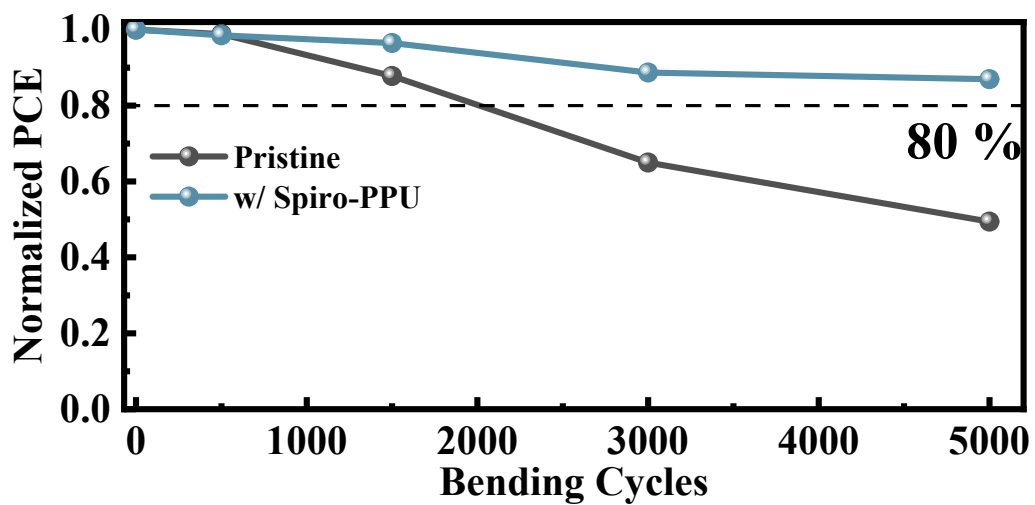


Fig. S34. Bending stability of flexible devices.

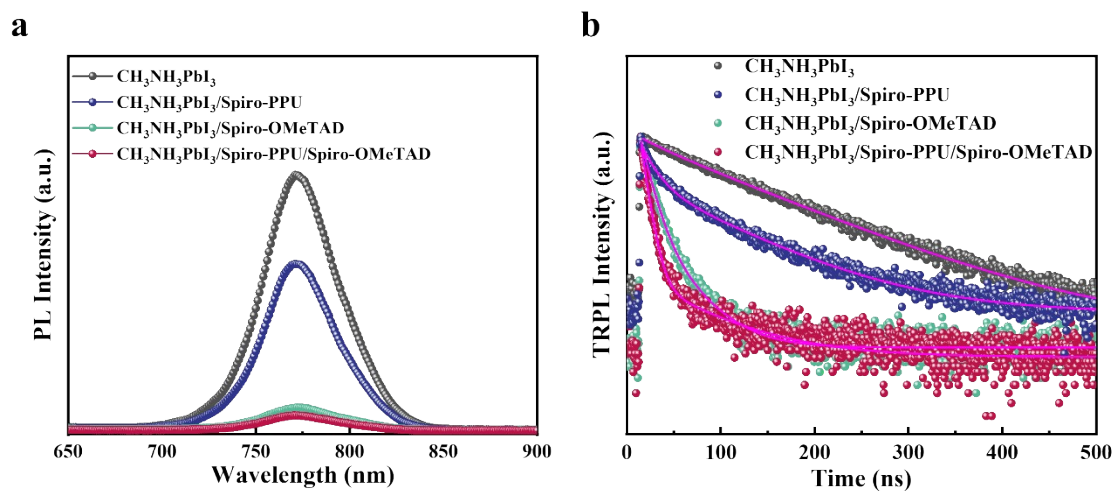


Fig. S35. (a) Steady-state PL and (b) TRPL spectra of the glass/ $\text{CH}_3\text{NH}_3\text{PbI}_3$, glass/ $\text{CH}_3\text{NH}_3\text{PbI}_3/\text{Spiro-PPU}$, glass/ $\text{CH}_3\text{NH}_3\text{PbI}_3/\text{Spiro-OMeTAD}$, and glass/ $\text{CH}_3\text{NH}_3\text{PbI}_3/\text{Spiro-PPU}/\text{Spiro-OMeTAD}$.

7. ^1H NMR, ^{13}C NMR and HR-MS spectra.

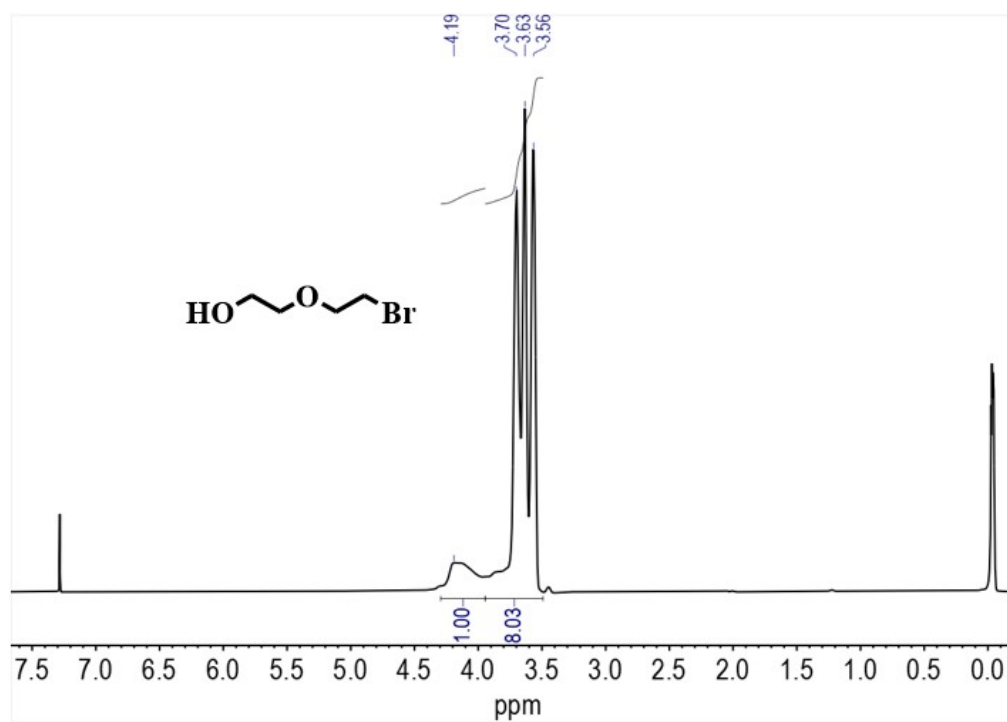


Fig. S36. ^1H NMR of compound (2).

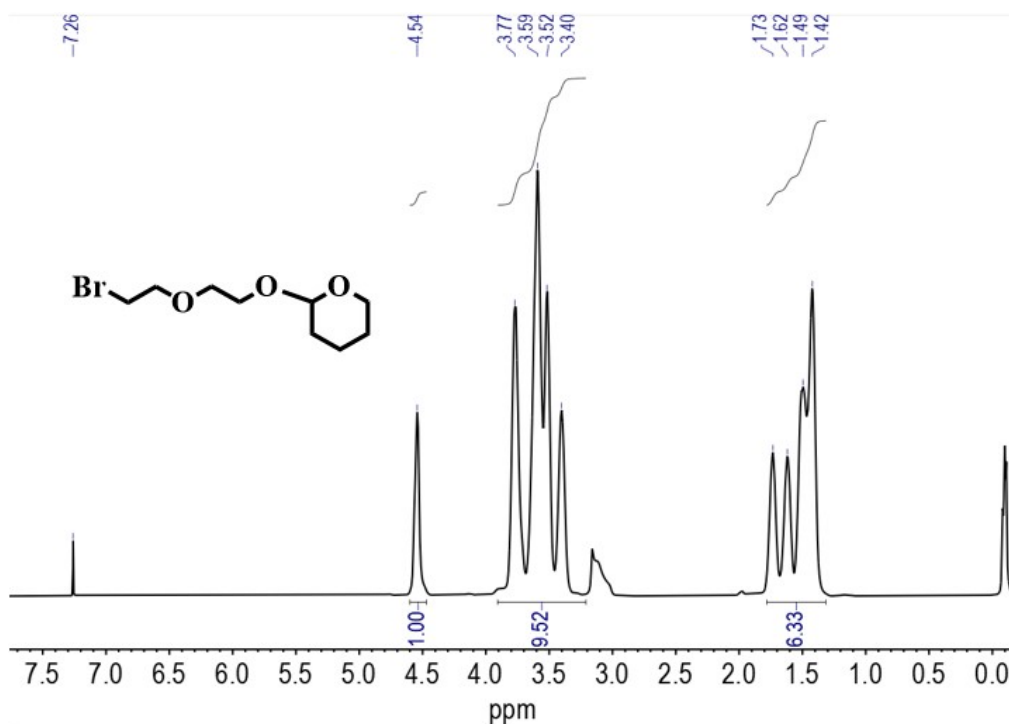


Fig. S37. ^1H NMR of compound (3).

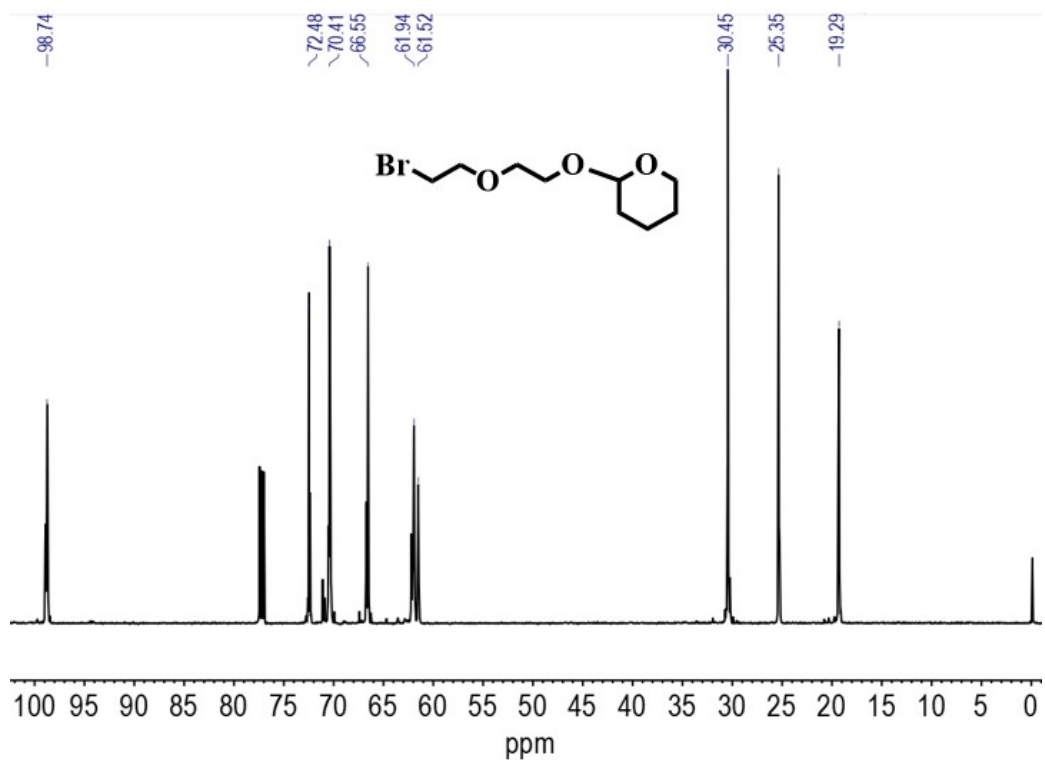


Fig. S38. ^{13}C NMR of compound (3).

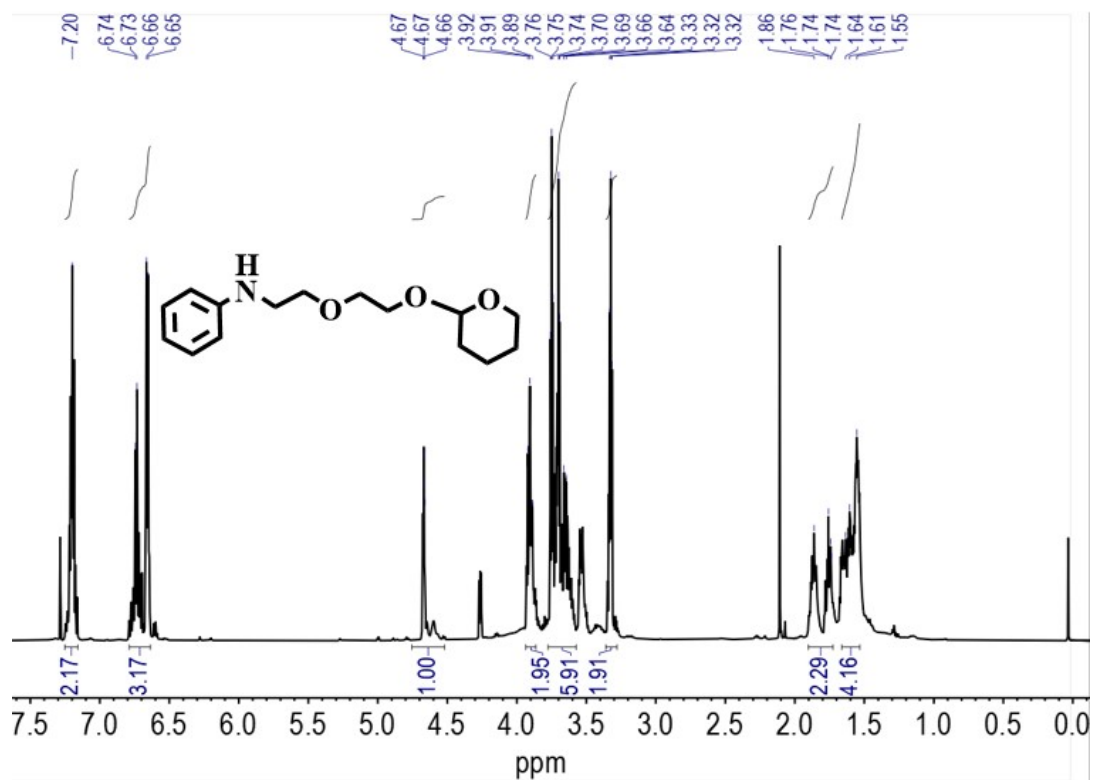


Fig. S39. ^1H NMR of compound (4).

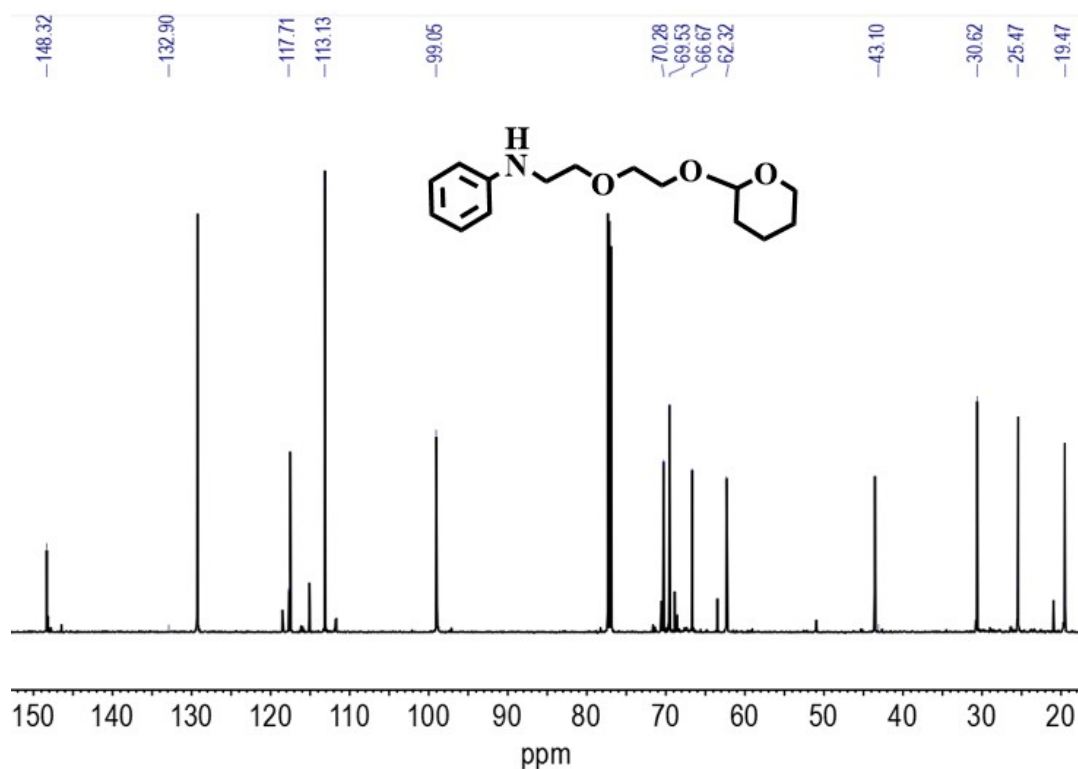


Fig. S40. ¹³C NMR of compound (4).

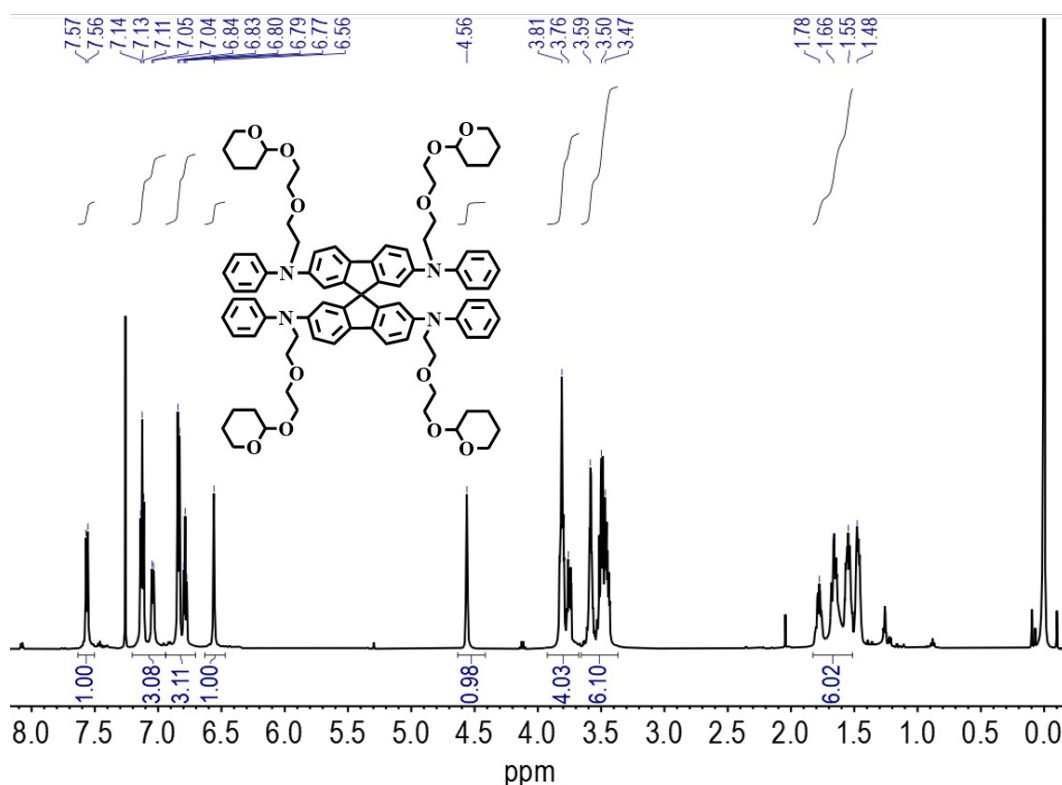


Fig. S41. ¹H NMR of compound (Spiro-ET).

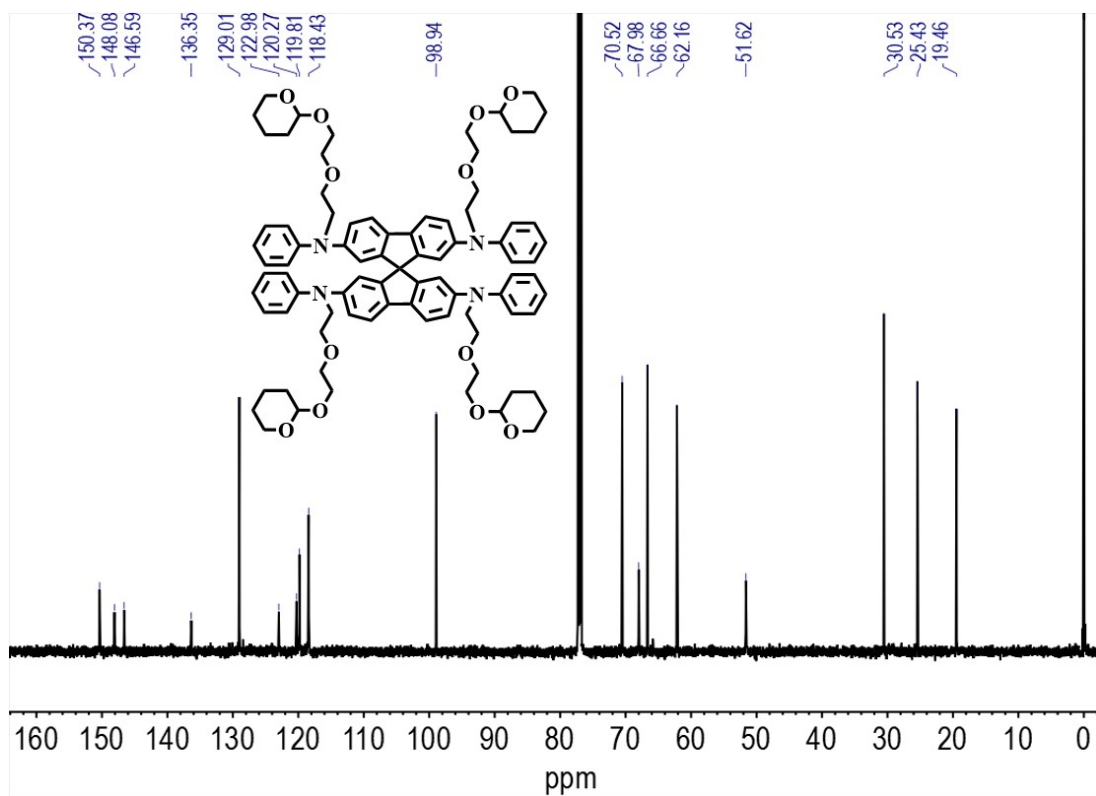


Fig. S42. ^{13}C NMR of compound (*Spiro-ET*).

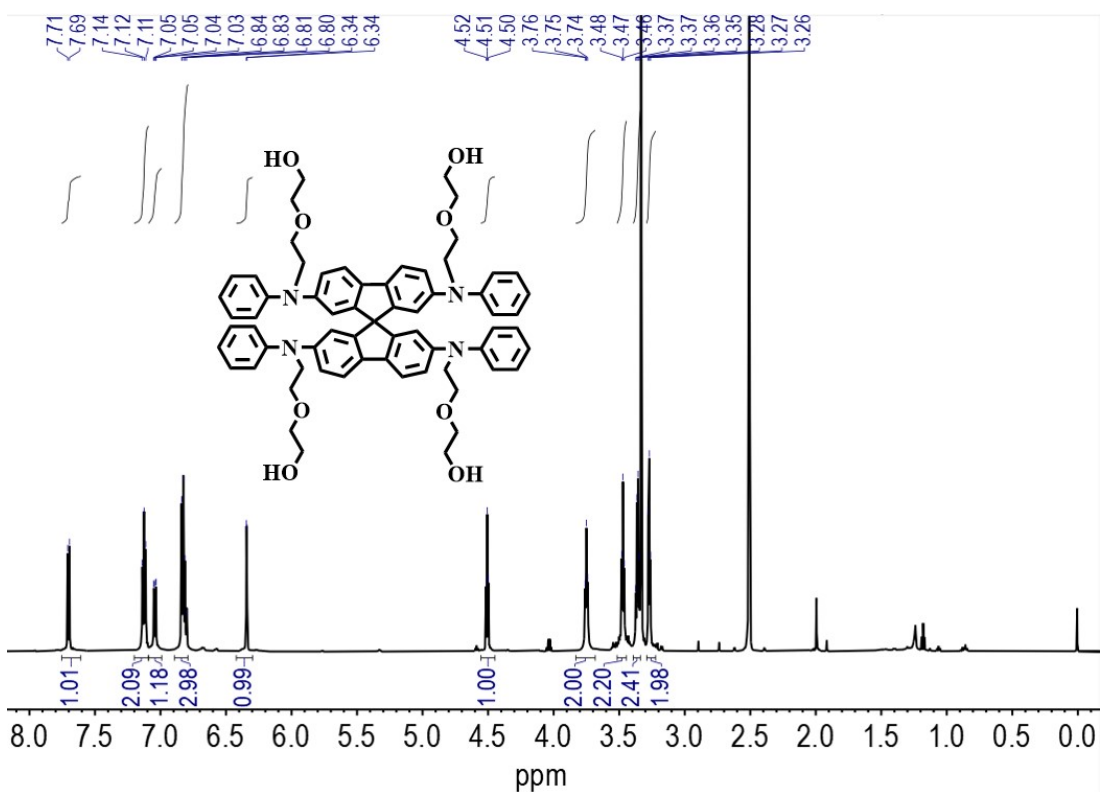


Fig. S43. ^1H NMR of compound (*Spiro-OH*).

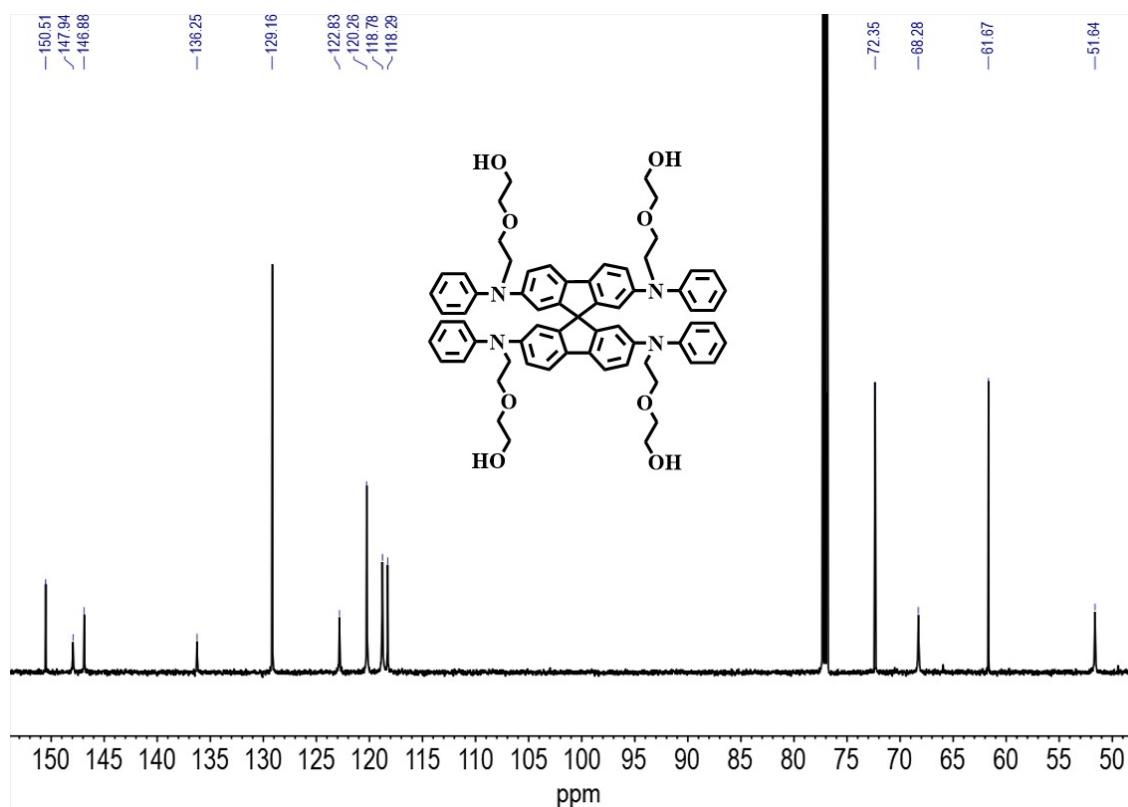


Fig. S44. ^{13}C NMR of compound (*Spiro-OH*).

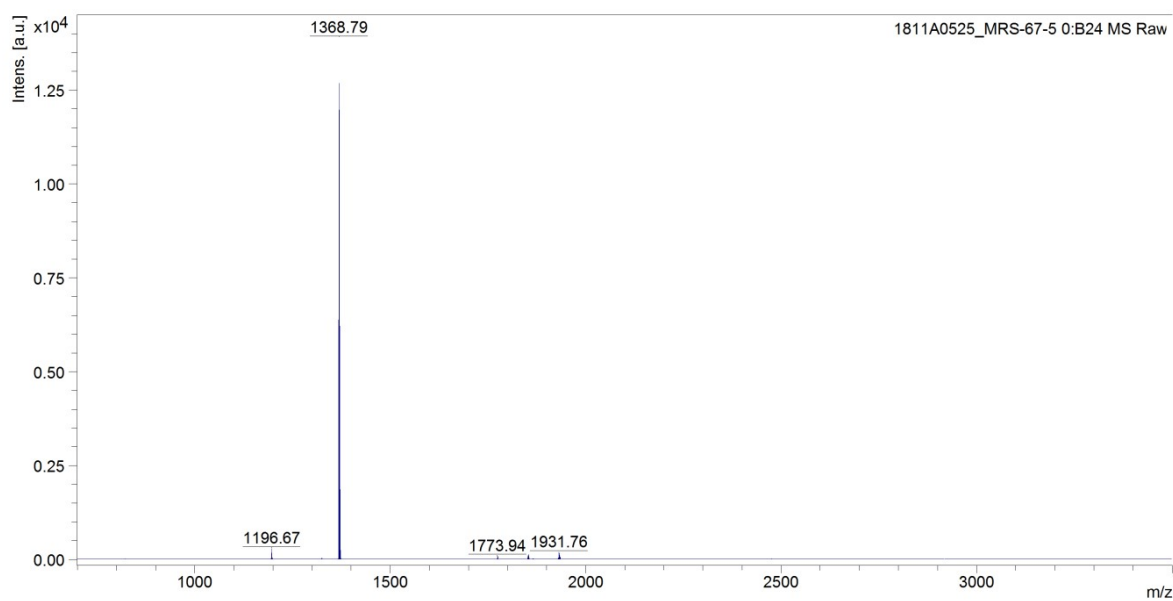


Fig. S45. HR-MS of compound (*Spiro-ET*).

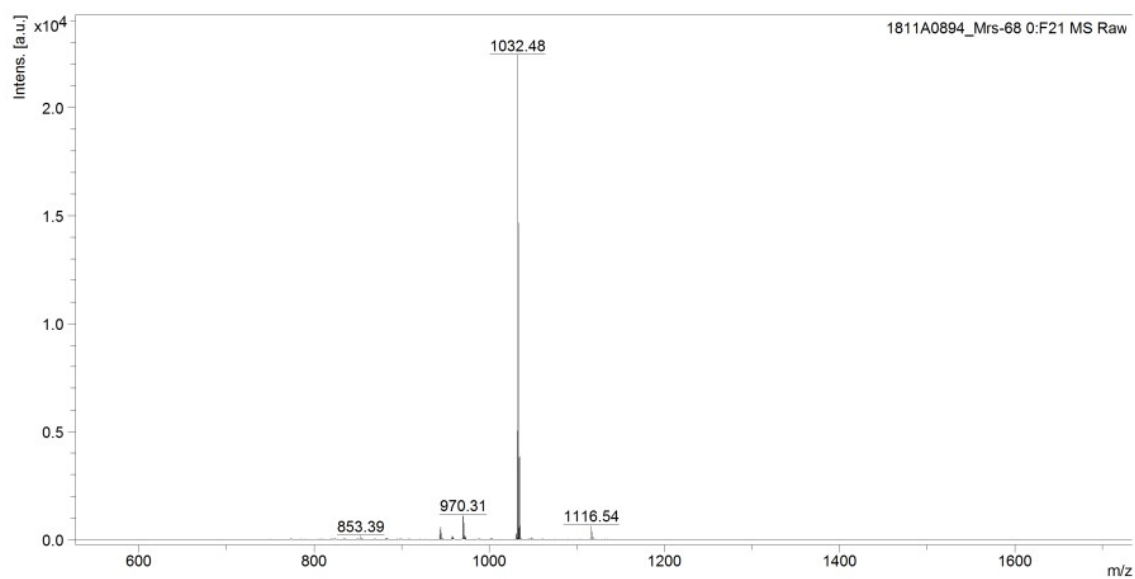


Fig. S46. HR-MS of compound (*Spiro-OH*).

- 1 Chen, C. *et al.* Solvent-Assisted Low-Temperature Crystallization of SnO₂ Electron-Transfer Layer for High-Efficiency Planar Perovskite Solar Cells. *Adv. Funct. Mater.* **29**, 1900557 (2019).